Lithos 266–267 (2016) 64–86

Contents lists available at ScienceDirect

Lithos

journal homepage: www.elsevier.com/locate/lithos

Archean crustal evolution in the Southern São Francisco craton, Brazil: Constraints from U-Pb, Lu-Hf and O isotope analyses

Capucine Albert [a,*], Federico Farina [b], Cristiano Lana [a], Gary Stevens [c], Craig Storey [d], Axel Gerdes [e], Carmen Martínez Dopico [f]

[a] Departamento de Geologia, Universidade Federal de Ouro Preto, Morro do Cruzeiro, Ouro Preto 35400-000, MG, Brazil
[b] University of Geneva, Section of Earth and Environmental Sciences, 13 Rue des Maraichers, 1205 Geneva, Switzerland
[c] Department of Earth Sciences, Centre for Crustal Petrology, Stellenbosch University, Private Bag X1, Stellenbosch, Matieland 7602, South Africa
[d] School of Earth and Environmental Sciences, University of Portsmouth, Burnaby Building, Burnaby Rd, Portsmouth PO1 3QL, UK
[e] Institut für Geowissenschaften, Goethe-Universität Frankfurt, Altenhöferallee 1, D-60438 Frankfurt am Main, Germany
[f] Instituto de Geocronología y Geología Isotópica, CONICET, Universidad de Buenos Aires, Avenida Int. Güiraldes s/n, Ciudad Universitaria, Buenos Aires, Argentina

ARTICLE INFO

Article history:
Received 6 April 2016
Accepted 17 September 2016
Available online 18 October 2016

Keywords:
Crustal evolution
Zircon
U–Pb dating
Lu–Hf isotopes
O isotopes
São Francisco craton

ABSTRACT

In this study we present U–Pb and Hf isotope data combined with O isotopes in zircon from Neoarchean granitoids and gneisses of the southern São Francisco craton in Brazil. The basement rocks record three distinct magmatic events: Rio das Velhas I (2920–2850 Ma), Rio das Velhas II (2800–2760 Ma) and Mamona (2750–2680 Ma).

The three sampled metamorphic complexes (Bação, Bonfim and Belo Horizonte) have distinct ε_{Hf} vs. time arrays, indicating that they grew as separate terranes. Paleoarchean crust is identified as a source which has been incorporated into younger magmatic rocks via melting and mixing with younger juvenile material, assimilation and/or source contamination processes. The continental crust in the southern São Francisco craton underwent a change in magmatic composition from medium- to high-K granitoids in the latest stages, indicating a progressive HFSE enrichment of the sources that underwent anatexis in the different stages and possibly shallowing of the melting depth. Oxygen isotope data shows a secular trend towards high $\delta^{18}O$ (up to 7.79‰) indicating the involvement of metasediments in the petrogenesis of the high potassium granitoids during the Mamona event. In addition, low $\delta^{18}O$ values (down to 2.50‰) throughout the Meso- and Neoarchean emphasize the importance of meteoritic fluids in intra-crustal magmatism.

We used hafnium isotope modelling from a compilation of detrital zircon compositions to constrain crustal growth rates and geodynamics from 3.50 to 2.65 Ga. The modelling points to a change in geodynamic process in the southern São Francisco craton at 2.9 Ga, from a regime dominated by net crustal growth in the Paleoarchean to a Neoarchean regime marked by crustal reworking. The reworking processes account for the wide variety of granitoid magmatism and are attributed to the onset of continental collision.

1. Introduction

Zircon has been extensively used for geochronological and geochemical studies for the past decades. This is primarily due to its abundance in crustal rocks, its resistance to weathering, its ability to retain complex growth zoning and its ability to be precisely dated. Combined U-Pb, Lu-Hf and O isotope studies on zircons have been widely used to trace the evolution of the continental crust, particularly in the Archean (e.g. Dhuime et al., 2012; Kemp et al., 2009a; Naeraa et al., 2012; Pietranik et al., 2008; Zeh et al., 2009, 2014).

The southern São Francisco craton (SSFC) encompasses a typical segment of Archean/Paleoproterozoic continental crust. The basement consists of granitoid-gneiss complexes exposed within domelike structures, in contact with Neoarchean and Paleoproterozoic supracrustal sequences. The geology of the SSFC has been investigated for over three centuries, primarily for its significant economic resources, and is a key location for studying Archean crustal evolution in South America (e.g. Carneiro et al., 1997; Farina et al., 2015, 2016; Hartmann et al., 2006; Koglin et al., 2014; Lana et al., 2013; Machado and Carneiro, 1992; Machado et al., 1992, 1996; Moreira et al., 2016; Noce et al., 1998, 2005; Romano et al., 2013; Teixeira and Figueiredo, 1991; Teixeira et al., 1996). Although a substantial number of these studies have aimed to unravel the Archean magmatic history of the SSFC, researchers are only recently starting to use a more regional approach.

* Corresponding author.
E-mail address: capucine.albert@gmail.com (C. Albert).

http://dx.doi.org/10.1016/j.lithos.2016.09.029
0024-4937/

Geochronological studies have shown that several Meso- and Neoarchean magmatic pulses have led to the construction of this crustal segment, followed by an episode of crustal reworking leading to the emplacement of large K-rich granitoids and the subsequent stabilization of the SSFC (Lana et al., 2013; Romano et al., 2013). Farina et al. (2015) assembled a large geochemical database on rocks from the basement and showed that in the Neoarchean there was a pronounced change in the composition of the crust, with a transition from medium-K to high-K magmatism. These authors proposed that this transition reflected the onset of basin deposition followed by the reworking of these rocks in the lower crust. Previous studies, however, lack the support of isotopic data. In order to place better constraints on the late-Archean evolution of the SSFC, we present the first set of U-Pb, Lu-Hf and O isotope data on single zircon grains from the basement rocks. This type of combined dataset has proven a powerful tool for deciphering geodynamic processes, particularly from times and places from which other geological records are scarce or absent.

In this paper we present a comprehensive dataset of zircon Lu-Hf and O isotope analyses for 30 gneisses, granitoids and amphibolitic dikes from the SSFC. This allows us to address several questions with implications for the Neoarchean crustal evolution of the southern São Francisco craton:

(i) What were the mechanisms of crust formation?
(ii) What was the nature and importance of crustal recycling/reworking and crust-mantle interactions?

2. Geological setting

The São Francisco craton represents one of the oldest segments of continental crust exposed in South America. It is composed of several Archean to Paleoproterozoic blocks, thought to have amalgamated during the 2.2–1.9 Ga Transamazonian orogenic event, and is bounded on all sides by Neoproterozoic orogenic belts (Almeida et al., 1981; Barbosa and Sabaté, 2004; Teixeira and Figueiredo, 1991). The southern edge of the craton exposes a section of Archean and Paleoproterozoic crust, including the Quadrilátero Ferrífero mining district that hosts world-class iron and gold deposits (Dorr, 1969; Lobato et al., 2001).

The SSFC was formed during a succession of magmatic pulses spanning from 3200 to 2600 Ma, in part concomitant with the deposition of a greenstone belt sequence, the Rio das Velhas Supergroup. The latest magmatic event saw the emergence of a stable continental platform, enabling the deposition of a thick Paleoproterozoic succession of volcanic, sedimentary and chemical strata, including the Minas Supergroup (Carneiro, 1992; Lana et al., 2013; Machado et al., 1992; Romano et al., 2013; Teixeira et al., 1996) (Fig. 1). The Archean basement in the SSFC is exposed within dome-like bodies reaching several tens of kilometres across (e.g. the Bação and Bonfim complexes), separated by elongate troughs containing polydeformed, low-grade supracrustal sequences. Together, these complexes have a typical Archean dome-and-basin geometry (Alkmim and Marshak, 1998; Marshak et al., 1992, 1997).

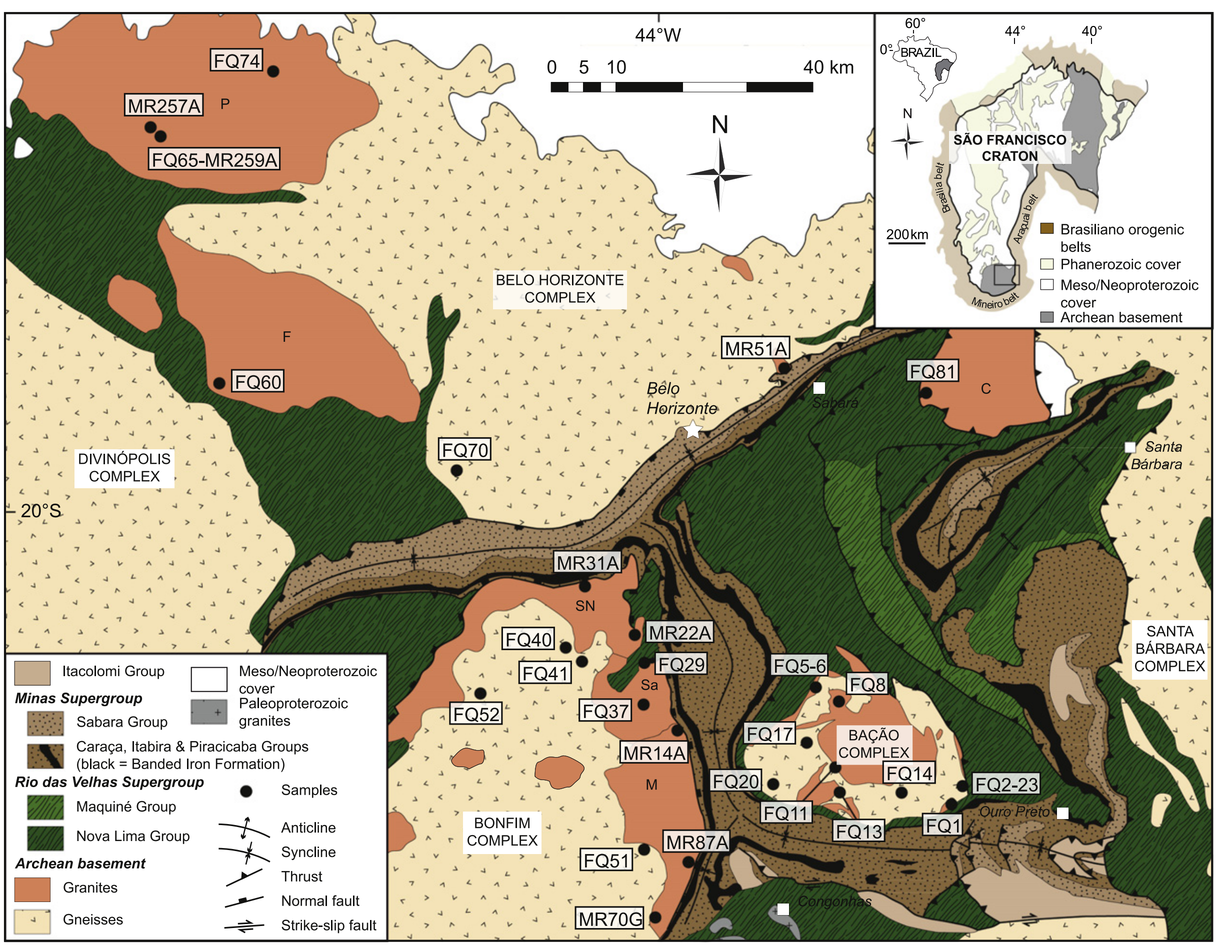

Fig. 1. Geological map of the southern São Francisco craton with sample locations. Abbreviations: F – Florestal, M – Mamona, P – Pequi, Sa – Samambaia, SN – Souza Noschese. Inset: simplified map of the São Francisco craton, showing the location of the exposed Archean provinces and the bordering Neoproterozoic orogenic belts. The box indicates the Quadrilátero Ferrífero.
Modified from Alkmim and Marshak (1998).

The Archean basement in the SSFC consists mainly of banded orthogneisses, intruded by several generations of granitoid bodies, leucogranitic sheets and dikes and late pegmatitic and aplitic veins. The gneisses display a complex pattern of amphibolite facies foliation, and locally exhibit stromatic migmatitic features (Lana et al., 2013). Lana et al. (2013) identified three main periods of magmatism in the SSFC, spanning between 3220 and 2770 Ma. Firstly, two gneisses cropping out in the south of the Santa Barbara complex were dated at 3212–3210 Ma, defining the eponymous Santa Barbara magmatic event. These ages are further supported by Sm-Nd T_{DM} model ages obtained by Teixeira et al. (1996) from medium- to high-grade gneisses located to the west of the SSFC (Campo Belo complex), and by a subset of detrital zircons from the Rio das Velhas and Minas Supergroups, suggesting the existence of fragments of Paleoarchean crust in the SSFC (Hartmann et al., 2006; Koglin et al., 2014; Machado et al., 1992, 1996; Moreira et al., 2016). The Rio das Velhas I and II (RVI and RVII) events are represented by gneisses and granitoids from the three main complexes (Bação, Bonfim and Belo Horizonte) yielding ages of 2920–2850 and 2800–2760 Ma respectively (Farina et al., 2015 and references therein). The widespread distribution of RVI and RVII rocks in and around the SSFC, and the presence in the detrital record of a large number of ca. 2800 and 2900 Ma zircon grains (Hartmann et al., 2006; Koglin et al., 2014; Moreira et al., 2016) emphasize the importance of the RVI and RVII as crust forming events.

The presence in the SSFC of several mostly undeformed granitoid batholiths dated at 2780–2770 Ma (namely the Samambaia and Caeté batholiths, Machado and Carneiro, 1992; Machado et al., 1992) indicates that the whole crust in the SSFC experienced regional metamorphism at the end of the RVII event. This crustal segment was later affected by one final magmatic event (namely the Mamona event; Farina et al., 2015), responsible for the production of voluminous granitoid batholiths, smaller granitic domains and leucogranitic sheets and dikes, intruded in and around the older gneissic-greenstone crust between 2750 and 2700 Ma (Machado et al., 1992; Noce et al., 1998; Romano et al., 2013). These large granitoid batholiths represent ~30% of the exposed surface of the SSFC (Romano et al., 2013). They are typically weakly foliated bodies, mostly encountered on the topographically higher outskirts of the Bonfim and Belo Horizonte complexes. In contrast, the older gneisses are found in the more eroded centre of the domes (Fig. 1). Noce et al. (1998) and Romano et al. (2013) also reported the occurrence in the south of the Bonfim complex of small granitoid bodies dated at 2613–2612 Ma. Romano et al. (2013) infer that these bodies account for less than 1% of the granitoid crust of the SSFC. In a recent contribution, Farina et al. (2015) provided the first detailed database of major and trace element compositions for gneisses and granitoids of the SSFC. These authors observed that the crust in the SSFC experienced a major compositional change during the Mamona event, shifting from medium- to high-K magmatism. As opposed to what several studies had previously assumed, Farina et al. (2015) demonstrated that the composition of the majority of the pre-Mamona intrusives does not match perfectly that of "true" Archean TTGs as described by Moyen (2011) ("true" TTGs refer to magmas that are formed via partial melting of an oceanic mafic crust, without any involvement from the continental crust). Instead, Farina et al. (2015) highlighted the "hybrid" nature of the medium-K rocks, which display whole rock major and trace element compositions that are intermediate between those of "true" TTGs and experimental melts derived from partial melting of TTGs, leading these authors to suggest an origin via mixing between an end-member derived by partial melting of metamafic crust and a component resulting from the reworking of older TTGs. On the other hand, the major and trace element compositions of the high-K granitoids argue in favour of derivation from low-degree partial melting of immature metasediments (e.g. metagreywacke). This transition was made possible by the continental emergence and appearance of sizeable clastic sedimentary basins in the Neoarchean (the Rio das Velhas greenstone belt), subsequently buried to provide the more fertile metasedimentary protoliths required for the petrogenesis of the high-K magmas. It is important to note that the crust of the Belo Horizonte complex does not record this transition from medium- to high-K magmatism. Indeed, the voluminous Pequi and Florestal batholiths intruded in the west during the Mamona event have compositional characteristics very similar to those of TTGs, testifying of a somewhat different evolution for that complex.

3. Analytical techniques

Zircon grains from 30 samples were analysed for Lu-Hf isotopes. For 9 samples, Lu-Hf was analysed on zircons previously dated by Farina et al. (2015). The remaining 21 samples were analysed for U-Pb during this study. Of these, 6 new samples were analysed, 8 samples previously studied by Romano et al. (2013) (labelled MR-) were re-dated using the same zircon mounts, and for the remaining 7 samples (previously dated by Farina et al. (2015)), further U-Pb analyses were done on additional zircons picked from the same zircon separate and mounted separately for O isotope analyses. These additional zircons were mounted together with the zircon standards Temora (Valley, 2003) and 91500 (Wiedenbeck et al., 2004) and care was taken during polishing in order to minimize the effects of sample geometry and topography (Kita et al., 2009). For this mount, the O isotope analyses were done prior to U-Pb and Lu-Hf analyses to ensure that the O data were not compromised by the laser pits.

U-Pb analyses were first conducted at the Universidade Federal de Ouro Preto (UFOP) during two analytical sessions: the first one in June-July 2013 using an Agilent 7700 Quadrupole (Q)-ICP-MS coupled to a New Wave UP213 ($\lambda = 213$ nm) Nd:YAG laser, while the second session was done between May 2014 and July 2015 using a Thermo-Scientific Element 2 Sector Field (SF) ICP-MS coupled to a CETAC LSX-213 G2+ ($\lambda = 213$ nm) Nd:YAG laser. U-Pb data reduction was done using the GLITTER® software package (Van Achterbergh et al., 2001). Concordia diagrams were generated using the Isoplot/Ex 4 program (Ludwig, 2003). Following each session of U-Pb dating, Lu-Hf isotope analyses were carried out during two analytical sessions, following the methods by Gerdes and Zeh (2006, 2009). The first one was performed in August 2013 using a multi-collector (MC)-ICP-MS Thermo-Finnigan Neptune system coupled to a Resonetics RESOlution M-50 193 nm Excimer laser at Goethe Universität Frankfurt (GUF) (Germany). The second session was conducted at UFOP between September 2014 and July 2015, using a multi-collector (MC)-ICP-MS Thermo-Scientific Neptune Plus system coupled to a Photon Machines 193 ($\lambda = 193$ nm) ArF Excimer laser ablation system. Oxygen isotopic compositions were determined by Secondary Ion Mass Spectrometry (SIMS) using a Cameca® IMS1270 multi-collector SIMS at the Edinburgh Materials and Micro-Analysis Centre (EMMAC, UK), following the methods described by Kemp et al. (2006, 2007). Laser spots for Lu-Hf analyses were drilled "on top" of the U-Pb and O spots or immediately beside, but always within the same zircon domain characterized by CL imaging.

The instrumental parameters used for U-Pb and Lu-Hf isotope analyses during both analytical sessions are shown in Table 1. A complete description of the analytical techniques is given in the Supplementary Material.

4. Results

A summary of all zircon U-Pb, Lu-Hf and O isotope data from this study is presented in Tables 2 and 3 and Figs. 2 and 3. Tables with the complete results are given in the Supplementary Material, along with concordia diagrams, zircon CL images and a full description of the geochronological data reduction applied for each sample. All uncertainties on the U-Pb analyses cited below are quoted at the 1σ level. All errors on the Lu-Hf analyses are quoted at the 2σ level.

Table 1
Operating conditions and instrumental settings for the U-Th-Pb and Lu-Hf analyses.

	U-Th-Pb Session 1	U-Th-Pb Session 2	Lu-Hf Session 1	Lu-Hf Session 2
Instrument	Agilent 7700	Element 2	Thermo-Finnigan Neptune	Thermo-Scientific Neptune +
Scan mode	E-Scan	E-Scan	Static	Static
Scanned masses	204, 206, 207, 208, 232, 238	202, 204, 206, 207, 208, 232, 238	172, 173, 175, 176, 177, 178, 179, 180	172, 173, 175, 176, 177, 178, 179, 180
Mass resolution	300	300	300	300
Dwell time	10 (204), 15 (206), 40 (207), 10 (208), 10 (232), 15 (238) ms	4 (202), 4 (204), 14 (206), 20 (207), 10 (208), 10 (232), 14 (238) ms	0.52 s	0.52 s
Integration time	0.9 s	0.9 s	1 s	1 s
Background	20 s	19 s	–	–
Ablation time	40 s	30 s	36 s	36 s
Carrier gas	1.0 L/min He (+1.0 L/min Ar)	0.5 L/min He (+1.0 L/min Ar)	0.6 L/min He (+0.9 L/min Ar, 0.007 L/min N)	1.3 L/min He (+1.0 L/min Ar, 0.15 L/min N)
Laser	213 nm New Wave	CETAC LSX-213 G2+	Resonetics RESOlution M-50	Photon Machines 193
Spot size	30 µm	20 µm	40 µm	40–50 µm
Laser settings	10 Hz, 6–8 J/cm^2	10 Hz, 3.5 J/cm^2	6 Hz, 4 J/cm^2	5 Hz, 3 J/cm^2
Cell volume	Low (teardrop)	Low (teardrop)	Low (two volume cell)	Low (two volume cell)

Zircon textures together with U-Pb analyses indicate that ca. 50% of the studied samples are characterized by magmatic zircon crystals that do not show metamorphic overgrowth. Zircon grains from these samples contain fine-grained oscillatory zoning patterns and yield well-defined U-Pb concordia or weighted mean ages. Moreover, all zircons, including those affected by different degrees of Pb-loss within individual samples, have identical $^{176}Hf/^{177}Hf_t$ ratios, leading to nearly horizontal arrays when plotted versus time (Fig. 2). Zircons from ca. 30% of the samples show more complex structures in CL images, typically displaying core-rim relationships with bright zoned or homogeneous cores surrounded by darker rims either showing oscillatory zoning or, more rarely, structureless. The rims display similar to slightly higher $^{176}Hf/^{177}Hf_t$ ratios with respect to the related cores (Fig. 2), and were generally interpreted as related to a subsequent metamorphic event. The cores were either interpreted as reflecting the crystallization age of the sample (e.g. FQ2), or as inherited zircon xenocrysts either from the source (e.g. FQ14) or by assimilation during intrusion (e.g. FQ37). Finally, the remaining ca. 20% of the samples are characterized by homogeneously dark and/or structureless zircons in CL images. A subset of zircons display some locally recrystallized domains and/or disruption of concentric oscillatory zoning. Ages obtained from these grains were interpreted to date a later metamorphic event. Within individual samples, the Th/U ratios of the zircons can be highly variable, and ca. 75% of the grains have ratios between 0.2 and 0.7. Moreover, except for 2 samples (FQ2 and FQ23) which display a systematic difference between high-Th/U cores and low-Th/U rims, cores and rims have similar Th/U ratios. Based on these considerations, this ratio was not used as criteria to distinguish different domains within a single grain nor as an argument to interpret an age. When possible, the α-decay damage accumulation of the zircons was calculated following Murakami et al. (1991), and used as an indicator of the degree of metamictization of the grains. Zircons showing α-decay doses > 8×10^{15} α/mg are considered highly damaged and those analyses were discarded. Overall, 9 out of 202 spot analyses were discarded. The α-decay doses of the remaining analyses range from 0.29 to 7.62×10^{15} α/mg, with an average of 2.84×10^{15} α/mg, testifying of the general good preservation of the zircon magmatic/metamorphic ages.

4.1. Geochronological results

The majority of the samples analysed during this study have already been dated by several authors, (see Table 3). For the seven samples previously dated by Farina et al. (2015), and for which we have analysed additional zircons, we used the intrusion/metamorphic ages provided by these authors, because these were generally more concordant and more representative of the samples, because they were obtained from a larger number of grains. This is the case for samples FQ1 (2711 ± 3 Ma), FQ2 (2868 ± 10 Ma), FQ17 (2778 ± 2 Ma), FQ29 (2773 ± 2 Ma), FQ52 (metamorphic age; 2727 ± 11 Ma), FQ60 (2728 ± 16 Ma) and FQ74 (metamorphic age: 2638 ± 14 Ma). For five samples, the ages obtained during this study are identical, within error, to those from the literature. This is the case for samples FQ5 (2761 ± 11 Ma), MR31A (2716 ± 14 Ma), MR70G (2716 ± 6 Ma), MR259A (2721 ± 9 Ma) and MR51A (2708 ± 10 Ma) (Table 3). Five additional samples yielded slightly different ages than those obtained during previous studies (<1.5% age difference): FQ6 (2779 ± 4 Ma), MR22A (2715 ± 2 Ma), MR87A (2646 ± 9 Ma), MR14A (2715 ± 3 Ma) and MR257A (2723 ± 8 Ma) (Table 3). For one sample (FQ20), we were not able to reproduce the published geochronological data. This sample corresponds to sample D07A from Lana et al. (2013), who obtained a SHRIMP magmatic age of 2918 ± 9 Ma, and a poorly defined metamorphic age of 2775 Ma. FQ20 yielded a majority of dark and structureless zircons, with a concordia age of 2723 ± 3 Ma which we interpreted as a metamorphic age of the rock.

In addition, we provide new LA-ICP-MS U-Pb ages for three, so far undated rocks. These consist of a banded gneiss crosscut by numerous leucogranitic sheets and dikes (FQ8), and a migmatitic gneiss (FQ14) from the Bação complex, as well as a foliated granitoid from the Caeté dome (FQ81). Zircons from FQ8 mostly display dark structureless centers, yielding a concordia age of 2612 ± 10 Ma, interpreted as a metamorphic age. A subset of zircon grains contain bright banded- or oscillatory-zoned inherited cores. Four discordant analyses on these cores gave older apparent ages that plot on a regression line yielding an age of ca. 2770 Ma for the protolith of the gneiss. CL images from zircons from FQ14 revealed a majority of dark and featureless grains. Ca. 40% of the zircons contain bright inherited cores, surrounded by dark homogeneous rims. The cores yielded concordant ages ranging from 2925 to 3472 Ma, clustered in four main populations at 2933, 3202, 3358 and 3465 Ma, while the rims gave a concordia age of 2692 ± 4 Ma. Sample FQ81 was collected from a foliated granitoid exposed in the Caeté dome (FQ81), where Machado and Carneiro (1992) had obtained a zircon U-Pb TIMS crystallization age of 2776 +7/−6 Ma from an outcrop located several kilometres away. In CL images, zircons from FQ81 are mostly dark and structureless, and yielded a younger age of 2671 ± 10 Ma, interpreted as the age of a late metamorphic event.

Several samples analysed during this study yielded metamorphic ages significantly younger than the Mamona event in the SSFC (<2680 Ma). Several authors have previously reported similarly young metamorphic ages in the Passa Tempo complex, located south of the Bonfim complex (2622 Ma, Campos et al., 2003), as well as in the Belo Horizonte complex (2670–2638 Ma, Farina et al., 2015). It is important to note that some of these ages are contemporaneous to the magmatic ages obtained from small granitoid intrusions from the south of the SSFC (2612–2613 Ma, Noce et al., 1998; Romano et al., 2013). However, the significance of this spread of metamorphic ages remains elusive.

4.2. Lu-Hf isotopes

The *RVI event* is represented by four banded trondhjemitic gneisses, collected from the eastern Bação complex and the central Bonfim complex. The gneisses from the Bação complex yield $^{176}Hf/^{177}Hf_t$ of 0.28090–0.28110 (±0.00002) corresponding to superchondritic εHf_t values between +0.7 and +5. By contrast, the rocks from the Bonfim complex have significantly lower $^{176}Hf/^{177}Hf_t$ ratios (Fig. 2a). Sample FQ40 contains several zircon cores with Hf isotope ratios ($^{176}Hf/^{177}Hf_t = 0.28087 \pm 0.00002$) identical to those of the gneiss FQ41 cropping nearby ($^{176}Hf/^{177}Hf_t = 0.28090 \pm 0.00002$), which corresponds to subchondritic εHf_t values between −1.1 and −3.4.

The *RVII event* is represented by six samples, five of them were collected within the Bação complex. They consist of two biotite-bearing banded gneisses, a fine-grained plagioclase-rich gneiss and two weakly deformed Kfs-bearing granitoids collected from small domains within the gneisses. The last sample was collected in the eastern Bonfim complex within the Samambaia tonalite pluton, and consists of a medium-grained amphibole- and epidote-bearing granitoid. As for the RVI event, samples from the Bação complex yield systematically higher $^{176}Hf/^{177}Hf_t$ ratios (0.28095–0.28107 ± 0.00002) than those from the Bonfim complex (0.28090 ± 0.00002) (Fig. 2b). It is worth noting that most of the rocks of the Bação complex exhibit superchondritic but slightly less radiogenic εHf_t values than the RVI gneisses. Three samples from the Bação complex display clear core/rim relationships, with rims dating a regional metamorphic event affecting the complex during the Mamona event, and yielding average $^{176}Hf/^{177}Hf_t$ of about 0.28102, corresponding to $\varepsilon Hf_t \sim 1$. Four samples from the Bação complex contain inherited zircon cores dated between 2825 to 2920 Ma, with $^{176}Hf/^{177}Hf_t$ ratios overlapping those of the RVI gneisses, indicating the involvement of RVI rocks in the petrogenesis of RVII magmas.

The *Mamona event* is documented by twenty samples collected from the Bação, Bonfim and Belo Horizonte/Caeté complexes (Fig. 2). The rocks from the *Bação complex* consist of a small weakly-foliated biotite-poor granitic body intruded at the edge of the complex, two banded gneisses crosscut by numerous leucogranitic sheets and dikes and a migmatitic gneiss. Zircons from banded gneisses are mostly dark and structureless, interpreted as metamorphic. They yield $^{176}Hf/^{177}Hf_t$ ratios ranging from 0.28099 ± 0.00002 to 0.28102 ± 0.00003. These values are similar to those obtained for the biotite-poor granite, and correspond to εHf_t values from −1 to −6 (Fig. 2c). Many zircons from the migmatitic gneiss (FQ14) contain bright inherited cores, surrounded by dark homogeneous rims. The cores yielded variable $^{176}Hf/^{177}Hf_t$ ratios ranging from 0.28101 to 0.28085, corresponding to highly scattered superchondritic to subchondritic εHf_t values (Fig. 2c). The rims exhibit $^{176}Hf/^{177}Hf_t$ ratios of 0.28102 ± 0.00003, indistinguishable from those obtained for the banded gneisses and the granite.

The Mamona event in the *Bonfim complex* is represented by eight samples: two small leucogranitic bodies, two weakly foliated aerially extensive granitoid phases from the Mamona and Souza Noschese batholiths, two small foliated granitoid bodies, a banded trondhjemitic gneiss cropping out in the centre of the dome and an amphibolitic dike. Zircons from all the granitoids show simple magmatic zoning patterns. All but one sample (FQ51, with $^{176}Hf/^{177}Hf_t = 0.28103 \pm 0.00002$) have identical $^{176}Hf/^{177}Hf_t$ ratios of 0.28095 ± 0.00003 (Fig. 2d). Zircons from the gneiss yielded comparatively higher Hf ratios of ~0.28101, which corresponds to $\varepsilon Hf_t \sim 3.8$, and were interpreted by Farina et al. (2015) to date a metamorphic event. Zircons from the amphibolite sample display core/rim relationships. Hf ratios for the rims average 0.28096 which is identical to the values obtained for the majority of the granitoids from the complex, while those of the cores range from 0.28087 to 0.28096, which is similar to the values obtained for the RVI gneisses from the Bonfim complex.

The Mamona event in the *Belo Horizonte complex* is documented by seven samples: four plagioclase-rich granitoids collected from the Pequi and Florestal batholiths, one fine-grained banded gneiss exposed in the southern part of the complex, one Kfs-rich augen gneiss and a medium-grained leucogranite. One additional sample was collected from a foliated granitoid exposed in the Caeté dome (FQ81). These eight samples have $^{176}Hf/^{177}Hf_t$ ratios comprised between 0.28092 ± 0.00002 and 0.28098 ± 0.00002, which corresponds to εHf_t values comprised between −6.2 and −1.7 (Fig. 2e).

4.3. O isotopes

Oxygen isotopic ratios were measured for 75 zircon grains from seven samples representative of the three main magmatic events, for which isotopic compositions (U-Pb and Lu-Hf) had already been obtained. Ca. 20% of the analyses fall within the range of $\delta^{18}O$ values in equilibrium with mantle-derived rocks ($\delta^{18}O = 5.3 \pm 0.3‰$) (Fig. 3). Ca. 30% analyses record slightly higher, more evolved compositions (>5.6‰), with only 6 spots falling in the range of “supracrustal zircon” (6.5–7.5‰) as defined by Cavosie et al. (2005) (Fig. 3). This field indicates a range of magmatic $\delta^{18}O$ values that are elevated with respect to those from mantle zircons, thus requiring input from rocks whose compositions have been shifted towards higher $\delta^{18}O$ values by low-temperature processes at Earth's surface. The upper limit of the field is based on the absence in the Hadean and Archean zircon record of values with $\delta^{18}O > 7.5‰$. One exception is a grain from FQ52 yielding an anomalously high $\delta^{18}O$ value of 10.88 ± 0.35‰. This grain is euhedral and shows oscillatory growth zoning under CL, and has an apparent $^{207}Pb/^{206}Pb$ age of 2718 ± 17 Ma (96% concordant). This is much higher than the sample average, and higher than $\delta^{18}O$ reported in Archean zircons (<7.5‰). Although there was no apparent crack or fracture at the surface of the grain, we suggest that the heavy O isotope value might originate from post crystallisation processes, as the gneiss has undergone metamorphism during the Mamona event. The remaining 50% of the analyses yielded $\delta^{18}O$ values below the range of mantle values (<5.0‰). These low $\delta^{18}O$ values make up a significant proportion of the zircons analysed during the three magmatic events, with 15 spots

Table 2
Selection of representative analyses of U-Pb, Lu-Hf and O isotopes.

Sample spot																					
Lu-Hf	U-Pb [a]	O	Grain description [b]	α-Decay events/mg ($\times 10^{15}$ α/mg)	Th/U	^{204}(Hg + Pb)	$^{238}U/^{206}Pb$	1σ	$^{207}Pb/^{206}Pb$	1σ	Pb/Pb age (Ma)	1σ	Conc. (%)	$^{176}Lu/^{177}Hf$	2σ	$^{176}Hf/^{177}Hf_t$	2σ	ε_{Hft}	2σ	$\delta^{18}O_{VSMOW}$ (‰)	2σ
Bação complex																					
FQ1																					
14_1	*14*		p m os	4.81	0.46	21	2.031	0.015	0.1874	0.0017	2719	15	97.1	0.00159	11	0.280988	28	−1.7	1.0		
16_1	*16*		p m os	3.94	0.74	27	1.909	0.015	0.1869	0.0018	2715	16	100.0	0.00158	10	0.281087	39	1.8	1.4		
22_1	*22*		p m os	3.80	0.82	46	2.075	0.019	0.1854	0.0021	2702	19	96.5	0.00167	11	0.280995	22	−1.8	0.8		
39_1	*39*		p m os	5.08	0.36	31	1.952	0.015	0.1865	0.0021	2711	18	99.1	0.00173	11	0.281028	27	−0.4	1.0		
58b_1	*58*		p m os	2.96	0.34	9	1.917	0.017	0.1860	0.0024	2707	21	100.0	0.00088	6	0.280981	36	−2.2	1.3		
75_1	*75*		p m os	3.15	1.13	5	1.903	0.016	0.1872	0.0024	2718	21	100.1	0.00156	10	0.281024	26	−0.4	0.9		
12a_2	15	8	p m os		0.28	0	2.073	0.015	0.1853	0.0021	2701	19	96.4	0.00111	8	0.281004	38	−1.5	1.4	7.00	0.19
15a_2	18	7	p m os		0.24	474	2.331	0.016	0.1786	0.0024	2640	22	92.0	0.00187	11	0.281007	14	−2.9	0.5	6.42	0.18
15b_2	18	7	p m os		0.24	474	2.331	0.016	0.1786	0.0024	2640	22	92.0	0.00187	11	0.281013	20	−2.6	0.7	6.42	0.18
17a_2	19	6	p m os		0.80	568	3.431	0.025	0.1665	0.0019	2522	19	74.4	0.00144	16	0.280960	24	−7.3	0.8	4.11	0.30
16a_2	21		p m os		0.66	239	2.329	0.017	0.1816	0.0020	2667	18	91.4	0.00124	9	0.280951	16	−4.2	0.6		
16b_2	22		p m os		0.60	0	3.258	0.024	0.1661	0.0019	2519	19	77.5	0.00109	7	0.280966	33	−7.1	1.2		
18a_2	29		p m os		0.59	529	2.136	0.018	0.1863	0.0028	2710	25	94.7	0.00175	11	0.280950	16	−3.3	0.6		
18b_2	29		p m os		0.59	529	2.136	0.018	0.1863	0.0028	2710	25	94.7	0.00121	8	0.280927	19	−4.1	0.7		
20a_2	30	5	p m os		0.44	150	2.816	0.020	0.1671	0.0018	2528	18	85.1	0.00094	6	0.280998	17	−5.8	0.6	6.24	0.21
21a_2	32	3	p m os		0.56	292	7.198	0.058	0.1311	0.0017	2112	23	48.0	0.00151	11	0.281022	25	−14.6	0.9	4.76	0.21
23b_2	34	4	p m os		0.04	60	2.916	0.024	0.1687	0.0023	2544	22	82.8	0.00182	13	0.280963	25	−6.7	0.9	5.28	0.22
22a_2	37	1	p m os		0.17	494	4.503	0.031	0.1248	0.0015	2026	21	76.4	0.00272	19	0.281014	17	−16.9	0.6	7.34	0.19
26b_2	43	11	p m os		0.18	581	6.552	0.050	0.1389	0.0019	2213	23	48.6	0.00205	13	0.281023	18	−12.2	0.6	5.75	0.26
24b_2	47	12	p m os		0.71	0	2.778	0.026	0.1696	0.0040	2554	38	85.2	0.00135	8	0.281014	22	−4.6	0.8	4.65	0.27
25b_2	47	12	p e os		0.71	0	2.778	0.026	0.1696	0.0040	2554	38	85.2	0.00128	8	0.281016	17	−4.5	0.6	4.65	0.27
13a_2	49		p e os		0.58	287	4.967	0.036	0.1451	0.0017	2289	20	61.4	0.00122	7	0.280998	20	−11.4	0.7		
FQ2																					
24_1	*24*		p m os	2.95	0.51	13	1.7792	0.014	0.2059	0.0022	2874	17	100.0	0.00418	35	0.281020	28	3.1	1.0		
27a_1	*27*		p m os	0.98	0.51	38	1.7739	0.017	0.2042	0.0026	2860	21	100.4	0.00167	11	0.281016	31	2.6	1.1		
27b_1	*27*		p m os	0.98	0.51	38	1.7739	0.017	0.2042	0.0026	2860	21	100.4	0.00079	5	0.280991	19	1.7	0.7		
43_1	*43*		p m os	0.80	0.34	28	1.7636	0.016	0.2090	0.0025	2898	19	100.0	0.00157	10	0.281006	19	3.2	0.7		
45_1	*45*		p m os	2.56	0.45	0	1.7983	0.014	0.2030	0.0020	2850	16	100.0	0.00241	15	0.281060	29	4.0	1.0		
53_1	*53*		p e rx	2.09	0.32	24	1.9291	0.020	0.1848	0.0032	2696	29	99.9	0.00134	10	0.281040	31	−0.4	1.1		
56b_1	*56*		p m os	2.37	0.52	3	1.7658	0.014	0.2083	0.0024	2892	18	100.0	0.00302	18	0.281050	23	4.6	0.8		
57_1	*57*		p m os	2.24	0.47	21	1.7874	0.015	0.2049	0.0022	2866	17	100.0	0.00245	15	0.280995	25	2.0	0.9		
61_1	*61*		p m os	2.39	0.44	0	1.7941	0.014	0.2033	0.0022	2853	18	100.1	0.00225	14	0.281037	18	3.2	0.6		
62_1	*62*		p m os	2.85	0.50	33	1.7864	0.015	0.2048	0.0022	2865	17	100.0	0.00196	12	0.281048	22	3.9	0.8		
67_1	*67*		p m os	2.34	0.59	41	1.7683	0.016	0.2078	0.0027	2888	21	100.0	0.00523	34	0.281106	25	6.5	0.9		
69_1	*69*		p m os	2.67	0.46	14	1.7902	0.014	0.2044	0.0020	2861	16	100.0	0.00315	34	0.280978	35	1.3	1.3		
70_1	*70*		an e os	2.87	0.03	12	1.9301	0.018	0.1843	0.0031	2692	27	100.0	0.00246	44	0.281018	34	−1.3	1.2		
71_1	*71*		p e os	4.79	0.02	0	2.8981	0.027	0.1718	0.0023	2575	22	84.9	0.00269	21	0.281035	25	−3.4	0.9		
73_1	*73*		ov m h	2.50	0.47	9	1.7879	0.015	0.2045	0.0027	2862	21	100.0	0.00125	8	0.281018	17	2.7	0.6		
74_1	*74*		p m os	2.35	0.49	8	1.7894	0.014	0.2049	0.0023	2866	18	99.9	0.00294	18	0.281002	24	2.3	0.8		
75_1	*75*		p e rx	3.88	0.07	0	1.9289	0.016	0.1854	0.0021	2702	18	99.8	0.00262	24	0.281025	25	−0.8	0.9		
76_1	*76*		p e h	3.48	0.21	0	2.6047	0.022	0.1867	0.0027	2713	24	86.4	0.00242	20	0.281012	23	−1.0	0.8		
32_2	15	10	p m os		0.21	163	3.0019	0.024	0.1747	0.0021	2603	20	79.5	0.00191	12	0.280985	17	−4.5	0.6	3.93	0.22
40_2	19		ov m os		0.28	53	2.1265	0.016	0.1902	0.0022	2744	19	94.2	0.00115	7	0.281038	16	0.7	0.6		
41_2	26	11	p e rx		0.04	50	3.2286	0.023	0.1598	0.0018	2454	19	79.9	0.00109	7	0.281030	23	−9.4	0.8	4.80	0.20
42_2	28	12	p m os		0.36	36	2.3211	0.017	0.1880	0.0021	2724	18	90.2	0.00257	23	0.281018	23	−0.5	0.8	4.64	0.14
39_2	32	1	p e rx		0.03	186	7.0636	0.057	0.0910	0.0013	1446	28	78.7	0.00175	12	0.281060	22	−28.6	0.8	3.11	0.19
37_2	39	2	p m os		0.42	0	1.9508	0.018	0.2033	0.0033	2853	26	96.0	0.00233	16	0.281034	22	3.1	0.8	3.06	0.14
36_2	40		p m os		0.24	81	2.3268	0.018	0.1807	0.0023	2659	21	91.6	0.00267	17	0.280989	33	−3.1	1.2		
35_2	44	6	p e rx		0.02	0	3.0307	0.022	0.1621	0.0019	2478	20	82.6	0.00112	7	0.281076	20	−4.2	0.7	3.77	0.21

(continued on next page)

Table 2 (*continued*)

Sample spot																					
Lu-Hf	U-Pb [a]	O	Grain description[b]	α-Decay events/mg ($\times 10^{15}$ α/mg)	Th/U	^{204}(Hg + Pb)	$^{238}U/^{206}Pb$	1σ	$^{207}Pb/^{206}Pb$	1σ	Pb/Pb age (Ma)	1σ	Conc. (%)	$^{176}Lu/^{177}Hf$	2σ	$^{176}Hf/^{177}Hf_t$	2σ	ε_{Hft}	2σ	$\delta^{18}O_{VSMOW}$ (‰)	2σ
27_2	46		p m os		0.43	0	1.9391	0.017	0.2036	0.0032	2855	25	96.3	0.00189	14	0.281019	24	2.6	0.9		
29_2	48	8	p e os		0.04	95	2.7267	0.020	0.1649	0.0020	2507	21	87.4	0.00170	10	0.281019	41	−5.6	1.4	4.62	0.14
FQ13																					
23	*23*		p c h	5.80	0.32	10	1.7194	0.013	0.2093	0.0017	2900	13	101.1	0.00181	11	0.280883	26	−1.2	0.9		
26	*26*		p m h	1.33	0.49	0	1.8431	0.018	0.1965	0.0026	2797	22	100.0	0.00127	8	0.281030	27	1.6	1.0		
28	*28*		p m os	1.98	0.67	22	1.8597	0.016	0.1957	0.0018	2790	15	99.7	0.00133	10	0.281029	33	1.4	1.2		
33	*33*		p m os	1.30	0.56	13	1.9248	0.019	0.1854	0.0020	2702	18	99.9	0.00127	8	0.281036	30	−0.4	1.1		
34	*34*		p m h	0.90	0.57	22	1.8415	0.016	0.1953	0.0021	2788	17	100.2	0.00088	6	0.281010	22	0.7	0.8		
38	*38*		p m os	1.49	0.68	7	1.8400	0.015	0.1964	0.0018	2796	15	100.0	0.00143	9	0.281059	29	2.7	1.0		
39	*39*		p m os	0.87	0.52	9	2.0158	0.019	0.1832	0.0022	2682	20	98.2	0.00100	8	0.281046	25	−0.5	0.9		
49	*49*		p m os	2.24	0.34	5	1.8515	0.015	0.1947	0.0018	2783	15	100.0	0.00082	8	0.281022	23	1.0	0.8		
50	*50*		p m os	5.44	0.41	27	1.8452	0.016	0.1947	0.0016	2783	14	100.2	0.00079	10	0.281027	21	1.2	0.8		
57	*57*		p m h	3.00	0.11	3	1.8375	0.015	0.1969	0.0016	2800	14	100.0	0.00081	7	0.280945	15	−1.3	0.6		
58	*58*		p m h	3.83	0.09	22	1.8238	0.015	0.1968	0.0016	2800	14	100.4	0.00084	7	0.280909	21	−2.6	0.7		
59	*59*		p m os	1.11	0.58	26	1.8363	0.016	0.1938	0.0020	2775	17	100.6	0.00118	8	0.281044	30	1.6	1.1		
61	*61*		p m os	1.49	0.69	19	1.8431	0.015	0.1958	0.0020	2791	16	100.1	0.00189	13	0.281075	31	3.1	1.1		
68	*68*		p m h	1.67	0.67	9	1.8433	0.015	0.1959	0.0018	2792	15	100.0	0.00129	9	0.281049	27	2.2	1.0		
72	*72*		p m os	0.65	0.39	0	1.8428	0.020	0.1958	0.0027	2791	23	100.1	0.00140	14	0.281025	34	1.3	1.2		
83	*83*		p m os	1.25	0.56	7	1.7996	0.015	0.1964	0.0020	2796	17	101.1	0.00132	8	0.281052	17	2.4	0.6		
84	*84*		p m os	1.33	0.64	14	1.8645	0.016	0.1930	0.0019	2768	16	100.0	0.00100	8	0.281032	23	1.0	0.8		
FQ17																					
10aI_1	*10_a*		ov m os	5.40	0.06	23	1.9114	0.017	0.1883	0.0018	2727	16	99.7	0.00125	9	0.281062	30	1.1	1.1		
10bI_1	*10_a*		ov m os	5.40	0.06	23	1.9114	0.017	0.1883	0.0018	2727	16	99.7	0.00102	9	0.281056	28	0.9	1.0		
11I_1	*11_a*		eq m os	5.76	0.05	5	1.9041	0.015	0.1893	0.0019	2736	17	99.7	0.00082	5	0.281060	27	1.3	1.0		
14I_1	*14_a*		p m os	5.13	0.05	9	1.9076	0.015	0.1874	0.0018	2719	16	99.9	0.00067	4	0.281015	22	−0.7	0.8		
15I_1	*15_a*		p m os	0.46	0.33	0	1.9055	0.030	0.1884	0.0043	2728	37	99.8	0.00044	3	0.280999	23	−1.1	0.8		
19II_1	*19_b*		p e os	4.00	0.07	12	1.9006	0.015	0.1881	0.0018	2726	16	100.0	0.00036	2	0.281035	18	0.2	0.7		
23I_1	*23_a*		p m os	6.40	0.43	16	1.8891	0.015	0.1896	0.0017	2739	15	100.0	0.00061	4	0.280987	19	−1.2	0.7		
30I_1	*30_a*		p m os	5.40	0.35	9	1.8539	0.014	0.1941	0.0018	2778	15	100.1	0.00119	9	0.281014	22	0.6	0.8		
32I_1	*32_a*		p m os	1.48	0.06	6	1.8577	0.016	0.1944	0.0021	2780	17	99.9	0.00091	10	0.280963	17	−1.1	0.6		
33I_1	*33_a*		p m os	4.21	1.09	9	1.8560	0.015	0.1942	0.0019	2778	16	100.0	0.00110	11	0.280989	25	−0.3	0.9		
33II_1	*33_b*		p m os	4.55	0.20	20	1.9454	0.018	0.1850	0.0025	2698	22	99.5	0.00085	6	0.281018	29	−1.1	1.0		
35II_1	*35_b*		p c h	7.34	0.41	48	1.7840	0.015	0.2055	0.0022	2871	17	100.0	0.00166	14	0.280913	24	−0.8	0.9		
42I_1	*42_a*		p m h	3.64	0.25	59	1.8551	0.014	0.1946	0.0018	2782	15	99.9	0.00055	4	0.280979	20	−0.5	0.7		
43aII_1	*43_b*		p m h	3.10	0.16	25	1.9035	0.017	0.1874	0.0024	2720	21	100.0	0.00059	4	0.280999	21	−1.3	0.7		
43bII_1	*43_b*		p m h	3.10	0.16	25	1.9035	0.017	0.1874	0.0024	2720	21	100.0	0.00081	6	0.281006	15	−1.0	0.6		
50II_1	*50_b*		p c os	4.54	0.46	58	1.8170	0.015	0.1998	0.0024	2825	19	100.0	0.00094	6	0.280934	21	−1.1	0.7		
51II_1	*51_b*		p e h	7.38	0.54	24	1.8810	0.016	0.1906	0.0024	2747	20	100.0	0.00057	4	0.281000	18	−0.6	0.6		
52II_1	*52_b*		p m os	3.66	0.29	43	1.8892	0.016	0.1900	0.0021	2742	18	99.9	0.00076	5	0.281012	21	−0.3	0.7		
56II_1	*56_b*		p m os	4.33	0.36	3	1.8983	0.017	0.1910	0.0023	2751	19	99.5	0.00148	10	0.281045	22	1.1	0.8		
61II_1	*61_b*		p c h	2.28	0.33	46	1.7882	0.019	0.2039	0.0039	2858	31	100.1	0.00121	8	0.281032	19	3.2	0.7		
48_2	12	8	p m os		0.32	38	1.9276	0.015	0.1847	0.0020	2695	18	100.0	0.00071	6	0.281042	29	−0.3	1.0	5.76	0.15
47_2	14	7	p m h		0.51	310	3.3735	0.024	0.1841	0.0020	2690	18	70.0	0.00175	21	0.280988	18	−2.4	0.6	4.00	0.22
45_2	15	5	p e os		0.24	0	2.0449	0.016	0.1859	0.0030	2706	26	97.0	0.00113	7	0.281015	18	−1.0	0.6	6.29	0.19
46_2	16	6	p m os		0.39	160	2.4549	0.018	0.1755	0.0019	2611	18	90.1	0.00072	6	0.280991	16	−4.1	0.6	5.46	0.21
44_2	17		p m os		0.63	83	1.9270	0.014	0.1865	0.0021	2711	18	99.7	0.00143	11	0.280985	18	−2.0	0.7		
43_2	18		p e os		0.04	157	2.0333	0.014	0.1868	0.0021	2714	18	97.0	0.00137	10	0.280998	18	−1.4	0.6		
52_2	19		p m os		0.36	153	1.8932	0.014	0.1870	0.0020	2716	17	100.4	0.00123	11	0.281003	23	−1.2	0.8		
50_2	21	4	p m os		0.25	378	1.9737	0.016	0.1871	0.0034	2717	30	98.4	0.00068	4	0.281013	19	−0.8	0.7	5.56	0.15
51_2	21	4	p e os		0.25	378	1.9737	0.016	0.1871	0.0034	2717	30	98.4	0.00146	10	0.281007	21	−1.1	0.8	5.56	0.15
54_2	30		p m os		0.24	441	1.9255	0.015	0.1869	0.0027	2715	24	99.6	0.00104	7	0.280999	20	−1.4	0.7		
56_2	35	3	p m os		0.13	619	2.0030	0.016	0.1961	0.0024	2794	20	96.0	0.00196	12	0.280988	21	0.1	0.7	4.88	0.20
55_2	36		p m os		0.35	193	2.0845	0.017	0.1859	0.0028	2706	24	96.0	0.00086	6	0.280983	34	−2.2	1.2		
57_2	38		p m os		0.41	190	1.8980	0.014	0.1945	0.0023	2781	19	98.9	0.00098	6	0.281012	25	0.6	0.9		

58_2	39		p e os	0.03	62	1.9543	0.014	0.1861	0.0021	2708	18	99.1	0.00066	4	0.281019	25	−0.8	0.9		
59_2	41	10	p m os	0.29	78	2.1471	0.016	0.1979	0.0024	2809	20	92.2	0.00124	10	0.280919	19	−2.0	0.7	5.98	0.15
63_2	42	11	p m os	0.25	10	1.9787	0.016	0.1869	0.0026	2715	23	98.4	0.00089	7	0.280985	18	−1.9	0.7	6.10	0.19
65_2	49		p m h	0.21	358	2.7349	0.020	0.1865	0.0027	2712	23	81.7	0.00252	16	0.280950	19	−3.1	0.7		
64_2	50	2	p e os	0.06	6	2.5948	0.019	0.1778	0.0024	2632	22	86.6	0.00090	6	0.280981	19	−4.0	0.7	5.01	0.23
66_2	52	1	p m os	0.04	46	2.7391	0.020	0.1844	0.0022	2692	20	82.1	0.00075	5	0.280995	15	−2.1	0.5	5.66	0.18
67_2	53		p m os	0.22	571	1.9676	0.015	0.1978	0.0028	2808	23	96.6	0.00294	18	0.281002	22	0.9	0.8		
Bação complex																				
FQ17																				
68_2	55		p m os	0.17	0	2.0438	0.015	0.1857	0.0022	2705	20	97.0	0.00080	7	0.280994	25	−1.8	0.9		
69_2	58	12	p m h	0.11	690	2.4740	0.022	0.1811	0.0035	2663	31	88.4	0.00183	12	0.281011	13	−2.2	0.5	4.49	0.18
70_2	65		p m h	0.68	128	2.3516	0.017	0.2004	0.0025	2829	20	86.9	0.00066	5	0.280970	16	0.3	0.6		
71_2	66		p e os	0.15	0	2.5148	0.018	0.1778	0.0024	2632	22	88.3	0.00087	6	0.280974	18	−4.2	0.6		
60_2	68	9	p m os	0.21	80	3.4464	0.025	0.1700	0.0022	2558	21	73.0	0.00079	7	0.280985	21	−5.6	0.8	5.59	0.19
61_2	71		p m os	0.32	377	1.9187	0.015	0.1968	0.0028	2800	23	98.0	0.00097	8	0.280999	17	0.6	0.6		
Bonfim complex																				
FQ29																				
20_2a	*15*		p m os	0.31	24	2.0304	0.016	0.1926	0.0021	2764	18	96.1	0.00089	7	0.280883	15	−4.3	0.6		
19_2a	*16*		p m h	0.23	46	1.8707	0.015	0.1935	0.0021	2772	17	99.8	0.00072	5	0.280881	15	−4.2	0.5		
21_2a	*17*		p n os	0.21	0	1.8834	0.014	0.1949	0.0025	2784	20	99.2	0.00121	8	0.280917	21	−2.7	0.8		
23_2a	*21*		p m os	0.25	71	1.7063	0.013	0.1967	0.0025	2799	20	103.6	0.00134	9	0.280889	12	−3.3	0.4		
24_2a	*21*		p m os	0.25	71	1.7063	0.013	0.1967	0.0025	2799	20	103.6	0.00084	5	0.280895	16	−3.1	0.6		
49_2a	*31*		p m os	0.42	10	2.1532	0.016	0.1943	0.0025	2779	21	93.2	0.00153	11	0.280902	18	−3.3	0.6		
25_2a	*32*		p m os	0.30	80	1.8770	0.015	0.1917	0.0022	2757	18	99.9	0.00058	4	0.280907	13	−3.7	0.5		
26_2a	*33*		p m os	0.21	75	2.1377	0.016	0.1895	0.0024	2738	20	94.4	0.00137	9	0.280894	17	−4.6	0.6		
27_2a	*33*		p m os	0.21	75	2.1377	0.016	0.1895	0.0024	2738	20	94.4	0.00169	15	0.280902	19	−4.3	0.7		
29_2a	*34*		p m os	0.27	7	1.8559	0.015	0.1945	0.0021	2781	18	100.0	0.00129	8	0.280900	16	−3.4	0.6		
28_2a	*35*		p m os	0.22	0	1.8534	0.014	0.1947	0.0022	2782	18	100.0	0.00173	15	0.280901	17	−3.3	0.6		
30_2a	*36*		p m os	0.35	49	1.8528	0.015	0.1922	0.0021	2761	17	100.4	0.00138	8	0.280888	17	−4.3	0.6		
31_2a	*48*		p m os	0.56	36	1.8794	0.014	0.1929	0.0024	2767	20	99.7	0.00165	12	0.280902	22	−3.6	0.8		
36_2a	*50*		p m os	0.46	112	1.8526	0.016	0.1959	0.0027	2792	23	99.8	0.00111	8	0.280919	17	−2.4	0.6		
34_2a	*52*		p e os	0.26	0	2.1081	0.018	0.1938	0.0028	2774	23	94.2	0.00078	5	0.280902	14	−3.5	0.5		
38_2a	*69*		p m os	0.42	32	2.5144	0.023	0.1939	0.0039	2776	33	86.6	0.00124	10	0.280901	15	−3.5	0.5		
39_2a	*70*		p m os	0.28	0	2.0041	0.017	0.1926	0.0029	2765	24	96.7	0.00136	9	0.280897	16	−3.8	0.6		
72_2b	11		p e os	0.19	181	2.3455	0.014	0.1907	0.0020	2748	17	89.0	0.00130	8	0.280922	24	−3.4	0.8		
73_2b	16		p e os	0.17	481	2.3599	0.014	0.1940	0.0021	2776	18	88.0	0.00082	6	0.280922	18	−2.7	0.6		
74_2b	17		p m os	0.19	132	1.8802	0.013	0.1967	0.0025	2799	21	99.0	0.00142	9	0.280921	22	−2.2	0.8		
78_2b	19		p m os	0.19	220	2.0579	0.013	0.1953	0.0020	2787	17	94.8	0.00133	8	0.280917	27	−2.6	0.9		
77_2b	20		p m os	0.20	0	1.9227	0.012	0.1954	0.0020	2788	16	98.1	0.00169	10	0.280943	26	−1.7	0.9		
76_2b	21		p m os	0.21	106	2.4086	0.015	0.1903	0.0019	2745	16	87.7	0.00164	11	0.280915	22	−3.7	0.8		
75_2b	26		p m os	0.17	357	1.8789	0.014	0.1958	0.0023	2792	19	99.1	0.00149	9	0.280928	20	−2.1	0.7		
12_2b	32		p m os	0.21	0	2.0933	0.013	0.1977	0.0021	2808	17	93.5	0.00224	17	0.280949	22	−1.0	0.8		
11_2b	34		p e os	0.18	365	2.6075	0.016	0.1910	0.0020	2750	17	83.2	0.00159	10	0.280908	17	−3.8	0.6		
80_2b	35	8	p m os	0.26	289	2.5051	0.016	0.1915	0.0020	2755	17	85.3	0.00112	7	0.280910	16	−3.6	0.6	4.95	0.23
16_2b	47	7	p e os	0.15	0	2.0930	0.013	0.1948	0.0020	2783	17	94.1	0.00145	9	0.280893	19	−3.6	0.7	5.29	0.25
15_2b	49		p m os	0.26	133	2.6635	0.017	0.1904	0.0021	2746	18	82.2	0.00147	9	0.280906	16	−4.0	0.6		
13_2b	51	9	p e os	0.19	312	2.1952	0.014	0.1981	0.0022	2811	18	91.0	0.00143	9	0.280905	16	−2.5	0.6	3.46	0.15
14_2b	53	10	p m os	0.23	226	2.0130	0.014	0.1947	0.0021	2782	18	95.9	0.00111	8	0.280886	17	−3.8	0.6	4.90	0.14
21_2b	59	11	p m os	0.15	324	1.9404	0.013	0.1966	0.0021	2798	17	97.5	0.00118	9	0.280915	18	−2.4	0.6	6.03	0.21
20_2b	62	14	p m os	0.12	177	1.9064	0.013	0.1966	0.0021	2799	17	98.3	0.00060	8	0.280972	16	−0.4	0.6	4.73	0.18
19_2b	64		p m os	0.19	0	2.1561	0.014	0.1987	0.0024	2815	19	91.8	0.00152	11	0.280924	23	−1.7	0.8		
18_2b	66	3	p m os	0.15	0	2.1031	0.014	0.1959	0.0021	2792	18	93.6	0.00124	11	0.280923	17	−2.3	0.6	5.23	0.26
27_2b	69	5	p m os	0.24	103	1.8554	0.013	0.1949	0.0022	2784	18	100.0	0.00142	9	0.280900	20	−3.3	0.7	4.86	0.15
28_2b	69	5	p m os	0.24	103	1.8554	0.013	0.1949	0.0022	2784	18	100.0	0.00160	12	0.280946	16	−1.7	0.6	4.86	0.15
25_2b	71	6	p m os	0.20	354	2.8988	0.020	0.1810	0.0020	2662	18	79.8	0.00125	8	0.280909	20	−5.8	0.7	5.80	0.14
26_2b	71	6	p m os	0.20	354	2.8988	0.020	0.1810	0.0020	2662	18	79.8	0.00100	6	0.280894	20	−6.4	0.7	5.80	0.14
24_2b	74	13	p m os	0.20	0	2.1463	0.014	0.1943	0.0021	2779	17	92.9	0.00118	8	0.280922	17	−2.6	0.6	5.04	0.22
22_2b	76		p m os	0.14	158	2.1085	0.014	0.1967	0.0022	2799	18	93.3	0.00134	8	0.280915	18	−2.4	0.6		

(continued on next page)

Table 2 (*continued*)

Sample spot																					
Lu-Hf	U-Pb [a]	O	Grain description [b]	α-Decay events/mg ($\times 10^{15}$ α/mg)	Th/U	^{204}(Hg + Pb)	$^{238}U/^{206}Pb$	1σ	$^{207}Pb/^{206}Pb$	1σ	Pb/Pb age (Ma)	1σ	Conc. (%)	$^{176}Lu/^{177}Hf$	2σ	$^{176}Hf/^{177}Hf_t$	2σ	ε_{Hft}	2σ	$\delta^{18}O_{VSMOW}$ (‰)	2σ
23_2b	77	12	p m os		0.18	144	1.7882	0.012	0.1990	0.0022	2818	18	101.0	0.00114	9	0.280907	19	−2.2	0.7	5.11	0.18
FQ41																					
14	*14*		p m os		0.25	134	2.0479	0.017	0.1988	0.0025	2816	19	94.7	0.00128	8	0.280883	18	−3.1	0.6		
13	*15*		p m os		0.32	51	1.8742	0.013	0.2029	0.0023	2850	18	98.1	0.00099	6	0.280890	21	−2.1	0.7		
15	*17*		p e os		0.29	133	2.4565	0.021	0.2009	0.0024	2834	19	86.5	0.00138	10	0.280907	20	−1.9	0.7		
16	*17*		p e os		0.29	133	2.4565	0.021	0.2009	0.0024	2834	19	86.5	0.00116	7	0.280912	16	−1.7	0.6		
12	*18*		p m os		0.39	63	2.1878	0.017	0.2034	0.0026	2853	20	91.0	0.00134	10	0.280908	19	−1.4	0.7		
19	*21*		p m os		0.31	58	1.8235	0.014	0.2029	0.0023	2850	18	99.4	0.00111	7	0.280903	17	−1.6	0.6		
17	*23*		p m os		0.34	138	2.0642	0.017	0.1957	0.0024	2791	19	94.8	0.00124	8	0.280885	25	−3.7	0.9		
18	*24*		p m os		0.38	53	2.2154	0.017	0.1981	0.0021	2810	17	91.3	0.00137	8	0.280919	19	−2.0	0.7		
20	*25*		p m os		0.27	241	2.4523	0.021	0.2039	0.0025	2857	20	86.1	0.00191	14	0.280899	14	−1.6	0.5		
23	*32*		p m os		0.38	17	2.4668	0.019	0.1955	0.0021	2789	18	87.2	0.00124	12	0.280908	27	−2.9	0.9		
22	*39*		p m os		0.29	43	1.9341	0.015	0.2029	0.0023	2850	18	96.6	0.00102	6	0.280909	25	−1.4	0.9		
25	*58*		p m os		0.39	55	1.8561	0.014	0.2024	0.0024	2846	18	98.6	0.00151	11	0.280894	21	−2.1	0.7		
26	*62*		p m os		0.25	88	1.8318	0.014	0.1970	0.0028	2802	22	100.1	0.00150	11	0.280886	22	−3.4	0.8		
27	*62*		p m os		0.25	88	1.8318	0.014	0.1970	0.0028	2802	22	100.1	0.00106	11	0.280906	18	−2.7	0.6		
28	*63*		eq m os		0.40	51	2.0871	0.016	0.2020	0.0024	2842	19	93.3	0.00120	8	0.280907	21	−1.7	0.7		
29	*66*		p e os		0.31	46	2.0283	0.015	0.2024	0.0029	2846	23	94.5	0.00105	7	0.280890	19	−2.2	0.7		
30	*67*		eq e os		0.24	10	1.8288	0.016	0.2055	0.0026	2870	21	98.8	0.00124	8	0.280867	17	−2.4	0.6		
FQ52																					
11_2a	*13_7*		p m h		0.26	0	1.8873	0.017	0.1903	0.0030	2745	26	99.9	0.00097	7	0.280995	19	−0.8	0.7		
12_2a	*13_7*		p m h		0.26	0	1.8873	0.017	0.1903	0.0030	2745	26	99.9	0.00102	10	0.280981	16	−1.3	0.6		
13_2a	*16_23*		p m os		0.35	47	2.0083	0.015	0.1895	0.0023	2738	19	97.2	0.00120	7	0.281002	19	−0.8	0.7		
15_2a	*17_7*		p m h		0.22	118	2.0043	0.021	0.1908	0.0032	2749	27	97.0	0.00060	4	0.280986	20	−1.1	0.7		
16_2a	*19_23*		p m os		0.21	5	1.8867	0.014	0.1905	0.0021	2747	18	99.9	0.00070	7	0.280983	18	−1.3	0.6		
17_2a	*21_23*		p m os		0.16	71	1.8939	0.015	0.1856	0.0020	2704	18	100.6	0.00079	5	0.280968	18	−2.7	0.6		
19_2a	*24_23*		p m os		0.26	0	1.9875	0.015	0.1887	0.0021	2731	18	97.8	0.00069	5	0.280966	20	−2.2	0.7		
26_2a	*44_23*		p e os		0.17	28	1.9433	0.017	0.1904	0.0024	2746	20	98.5	0.00083	5	0.280977	23	−1.4	0.8		
20_2a	*58_7*		p m os		0.26	41	1.9175	0.016	0.1876	0.0033	2721	28	99.7	0.00061	4	0.280996	20	−1.4	0.7		
21_2a	*61_7*		p m os		0.35	0	1.9482	0.018	0.1892	0.0036	2735	31	98.6	0.00073	5	0.281001	24	−0.8	0.8		
22_2a	*64_7*		p m h		0.17	7	1.8905	0.023	0.1900	0.0040	2742	34	99.9	0.00032	2	0.280970	19	−1.8	0.7		
27_2a	*83_7*		p m os		0.24	27	1.9622	0.020	0.1891	0.0041	2735	35	98.3	0.00086	10	0.281005	19	−0.7	0.7		
52_2b	18	6	p m os		0.67	193	2.0731	0.017	0.1873	0.0020	2718	17	96.0	0.00186	17	0.281015	29	−0.7	1.0	10.88	0.35
53_2b	18	6	p m os		0.67	193	2.0731	0.017	0.1873	0.0020	2718	17	96.0	0.00172	11	0.281031	21	−0.2	0.7	10.88	0.35
54_2b	20		p m os		0.74	133	2.1038	0.019	0.1872	0.0026	2718	23	95.4	0.00118	10	0.281018	31	−0.6	1.1		
56_2b	27	3	p m os		0.48	62	2.3487	0.018	0.1725	0.0019	2582	18	93.0	0.00176	11	0.281018	21	−3.8	0.7	4.48	0.29
55_2b	29	4	p m h		0.48	235	6.8733	0.054	0.1062	0.0012	1735	20	67.7	0.00150	24	0.281050	40	−22.3	1.4	2.88	0.29
58_2b	35	9	p m os		0.40	190	4.2757	0.035	0.1574	0.0017	2428	18	64.8	0.00142	12	0.281025	20	−7.2	0.7	4.17	0.31
59_2b	48	8	p m os		0.44	52	2.1764	0.019	0.1819	0.0023	2670	21	94.7	0.00066	4	0.280998	14	−2.5	0.5	6.73	0.34
60_2b	48	8	p m os		0.44	52	2.1764	0.019	0.1819	0.0023	2670	21	94.7	0.00121	10	0.281002	20	−2.3	0.7	6.73	0.34
61_2b	50		p m os		0.61	232	3.3519	0.026	0.1556	0.0018	2408	19	79.3	0.00165	14	0.281024	22	−7.7	0.8		
63_2b	52		p m rx		0.42	0	2.3087	0.021	0.1782	0.0024	2636	22	92.6	0.00134	9	0.281008	19	−2.9	0.7		
64_2b	53		p m rx		0.18	192	3.4598	0.028	0.1554	0.0020	2406	21	77.6	0.00106	10	0.281012	24	−8.2	0.9		
62_2b	54	14	p m os		0.62	265	4.4823	0.036	0.1464	0.0017	2305	19	66.6	0.00095	8	0.281085	22	−7.9	0.8	4.33	0.40
65_2b	57	12	p m os		0.56	457	2.9284	0.025	0.1696	0.0025	2553	24	82.4	0.00166	22	0.281042	24	−3.6	0.9	4.35	0.36
66_2b	62		p e os		0.76	503	3.1377	0.025	0.1666	0.0019	2524	19	79.4	0.00189	12	0.281000	20	−5.8	0.7		
48_2b	73	2	p m os		0.47	0	2.0209	0.017	0.1777	0.0025	2631	23	99.1	0.00177	15	0.281009	18	−3.0	0.6	6.33	0.44
49_2b	73	2	p m os		0.47	0	2.0209	0.017	0.1777	0.0025	2631	23	99.1	0.00070	5	0.280985	17	−3.9	0.6	6.33	0.44
51_2b	75	1	p m os		0.49	110	4.7192	0.039	0.1382	0.0020	2205	25	67.5	0.00207	20	0.281037	24	−11.9	0.9	4.46	0.39
MR14A																					
48	48		p m h	1.28	0.29	76	1.9897	0.017	0.1865	0.0018	2711	16	98.2	0.00048	3	0.280937	24	−3.7	0.8		
49	49		f c h	1.47	0.43	120	2.0806	0.018	0.2027	0.0021	2848	17	93.3	0.00054	4	0.280952	26	0.1	0.9		
54	54		f e os	2.82	0.28	54	1.9062	0.015	0.1869	0.0017	2715	15	100.1	0.00049	3	0.280912	21	−4.5	0.7		
56	56		f m h	3.54	0.29	34	2.0197	0.016	0.1860	0.0017	2707	15	97.6	0.00067	5	0.280975	25	−2.4	0.9		

58	58		f m os	1.89	0.29	40	1.9022	0.015	0.1867	0.0017	2714	15	100.2	0.00052	3	0.280956	33	−3.0	1.2		
70	70		p m os	3.49	0.40	100	1.9424	0.020	0.1888	0.0029	2731	25	98.9	0.00067	6	0.280970	29	−2.1	1.0		
71	71		f c os	2.02	0.42	184	1.9489	0.018	0.2248	0.0027	3016	19	93.0	0.00111	7	0.280910	24	2.5	0.9		
74	74		b m h	1.87	0.37	44	1.9268	0.017	0.1859	0.0029	2706	25	99.8	0.00123	9	0.280959	30	−3.0	1.1		
75	75		eq m h	1.26	0.36	36	1.9015	0.016	0.1881	0.0020	2726	18	100.0	0.00056	4	0.280975	33	−2.0	1.2		
Belo Horizonte complex																					
FQ60																					
15_2a	*145*		p m h		0.55	118	1.9164	0.015	0.1866	0.0022	2713	19	99.9	0.00070	5	0.280967	18	−2.6	0.7		
19_2a	*153*		p m h		0.31	312	2.4612	0.020	0.1832	0.0026	2682	23	89.4	0.00071	4	0.280968	20	−3.2	0.7		
20_2a	*159*		p m h		0.29	20	2.2232	0.017	0.1857	0.0023	2705	20	93.3	0.00084	5	0.280973	14	−2.5	0.5		
21_2a	*159*		p m h		0.29	20	2.2232	0.017	0.1857	0.0023	2705	20	93.3	0.00082	6	0.280948	18	−3.4	0.7		
22_2a	*160*		p m h		0.43	0	3.3584	0.029	0.1676	0.0021	2534	20	80.2	0.00056	4	0.280968	28	−6.7	1.0		
24_2a	*165*		p m os		0.33	154	1.9724	0.016	0.1735	0.0026	2592	23	101.1	0.00083	5	0.281000	29	−4.2	1.0		
25_2a	*166*		p m os		0.10	198	2.8405	0.023	0.1668	0.0023	2526	23	86.7	0.00084	7	0.280952	22	−7.5	0.8		
16_2a	*172*		p m h		0.54	0	1.9085	0.016	0.1883	0.0026	2728	23	99.8	0.00051	4	0.280964	18	−2.3	0.6		
71_2b	13	13	p m os		0.18	0	6.2996	0.049	0.1380	0.0016	2202	19	51.3	0.00140	14	0.281013	17	−12.9	0.6	2.86	0.33
69_2b	15		p e h		0.56	135	2.1648	0.017	0.1877	0.0022	2722	19	93.8	0.00073	5	0.281096	33	2.2	1.2		
72_2b	20		p m os		0.34	29	1.9434	0.016	0.1858	0.0023	2705	20	99.4	0.00100	6	0.280932	20	−4.0	0.7		
73_2b	30	1	f m os		0.22	337	2.8275	0.025	0.1884	0.0030	2728	26	79.3	0.00155	16	0.281011	22	−0.7	0.8	3.12	0.27
74_2b	34	5	p m os		0.30	577	4.3016	0.034	0.1864	0.0021	2710	18	53.7	0.00084	6	0.280957	25	−3.0	0.9	3.09	0.33
77_2b	43	14	f m os		0.30	144	1.9481	0.016	0.1859	0.0021	2706	19	99.3	0.00042	3	0.280921	20	−4.4	0.7	7.04	0.33
76_2b	44	15	f m os		0.29	22	1.9203	0.016	0.1855	0.0022	2703	19	100.0	0.00054	3	0.280924	22	−4.3	0.8	6.60	0.29
78_2b	45	7	ov c h		0.12	91	1.8973	0.016	0.1961	0.0024	2794	20	98.6	0.00025	3	0.280997	19	0.4	0.7	5.41	0.40
79_2b	46	8	ov c h		0.20	299	1.8430	0.016	0.1940	0.0026	2776	22	100.4	0.00028	2	0.280981	17	−0.6	0.6	5.34	0.37
11_2b	48		p m os		0.25	731	2.6782	0.022	0.1891	0.0024	2734	21	82.2	0.00118	7	0.280920	18	−3.7	0.6		
80_2b	50	4	p m os		0.25	310	3.8220	0.031	0.1723	0.0020	2580	19	66.1	0.00125	8	0.281000	25	−4.5	0.9	5.01	0.29
14_2b	54	9	p m os		0.22	266	5.0446	0.040	0.1547	0.0019	2399	20	56.0	0.00196	15	0.280985	17	−9.3	0.6	3.84	0.37
FQ74																					
18_2a	*16*		p m h		0.53	0	2.2873	0.018	0.1784	0.0022	2638	21	93.4	0.00066	5	0.280994	19	−3.4	0.7		
23_2a	*17*		b m h		0.69	197	2.4164	0.018	0.1620	0.0020	2477	18	94.5	0.00132	16	0.280942	15	−9.0	0.5		
21_2a	*18*		b m h		0.86	112	1.9859	0.016	0.1806	0.0021	2658	19	99.4	0.00077	11	0.280961	16	−4.1	0.6		
22_2a	*18*		b m h		0.86	112	1.9859	0.016	0.1806	0.0021	2658	19	99.4	0.00071	8	0.280957	18	−4.2	0.6		
25_2a	*20*		p m h		0.67	35	2.0394	0.017	0.1797	0.0022	2650	20	98.3	0.00100	7	0.280974	18	−3.8	0.6		
26_2a	*20*		p e h		0.67	35	2.0394	0.017	0.1797	0.0022	2650	20	98.3	0.00070	5	0.280997	16	−3.0	0.6		
19_2a	*34*		p m h		0.72	7	2.1548	0.018	0.1777	0.0022	2632	21	96.2	0.00122	13	0.280975	22	−4.2	0.8		
20_2a	*34*		p m h		0.72	7	2.1548	0.018	0.1777	0.0022	2632	21	96.2	0.00086	8	0.280963	20	−4.6	0.7		
16_2a	*35*		b m os		0.75	7	1.9880	0.015	0.1781	0.0022	2636	20	99.8	0.00120	9	0.281008	26	−2.9	0.9		
24_2a	*39*		p e os		0.73	4	2.1173	0.017	0.1791	0.0022	2644	20	96.7	0.00099	17	0.280961	23	−4.4	0.8		
27_2a	*43*		b e h		0.63	138	2.0353	0.016	0.1752	0.0020	2608	18	99.3	0.00075	6	0.280969	20	−5.0	0.7		
28_2a	*43*		b e h		0.63	138	2.0353	0.016	0.1752	0.0020	2608	18	99.3	0.00155	16	0.280966	22	−5.1	0.8		
29_2a	*55*		p m h		0.88	0	2.1397	0.024	0.1772	0.0035	2627	33	96.6	0.00141	20	0.280994	24	−3.6	0.9		
31_2a	*55*		p m h		0.88	0	2.1397	0.024	0.1772	0.0035	2627	33	96.6	0.00111	13	0.280960	18	−4.8	0.6		
32_2a	*74*		p m h		0.61	68	2.1565	0.020	0.1790	0.0031	2644	29	95.9	0.00119	9	0.280956	22	−4.6	0.8		
33_2a	*74*		p m h		0.61	68	2.1565	0.020	0.1790	0.0031	2644	29	95.9	0.00141	13	0.280954	20	−4.7	0.7		
38_2a	*96*		b m h		0.59	23	1.9935	0.016	0.1794	0.0026	2647	23	99.4	0.00115	14	0.280964	21	−4.2	0.7		
39_2a	*96*		b m h		0.59	23	1.9935	0.016	0.1794	0.0026	2647	23	99.4	0.00089	9	0.280959	20	−4.4	0.7		
33_2b	12		b m h		0.56	18	2.0267	0.022	0.1764	0.0030	2619	28	99.3	0.00098	7	0.280976	24	−4.5	0.9		
32_2b	14		b e os		0.32	66	3.0582	0.024	0.1597	0.0017	2452	18	82.9	0.00316	22	0.281004	22	−7.4	0.8		
31_2b	16		p m os		0.40	55	2.4930	0.020	0.1754	0.0020	2610	19	89.3	0.00134	9	0.280947	20	−5.7	0.7		
40_2b	19	14	p m os		0.16	407	4.1825	0.036	0.1869	0.0024	2715	21	55.4	0.00203	13	0.280980	15	−2.1	0.6	5.46	0.36
39_2b	26		p e os		0.51	361	2.6748	0.021	0.1709	0.0019	2566	18	86.8	0.00179	21	0.280968	19	−6.0	0.7		
38_2b	27		p m rx		0.41	0	2.0689	0.016	0.1752	0.0019	2608	18	98.6	0.00091	6	0.281022	11	−3.1	0.4		
37_2b	30		p m rx		1.08	0	2.6683	0.022	0.1757	0.0020	2613	18	85.7	0.00220	13	0.280991	13	−4.1	0.5		
36_2b	33	1	p m os		0.65	245	4.0358	0.034	0.1625	0.0019	2482	20	66.3	0.00136	9	0.280976	16	−7.7	0.6	4.45	0.32
45_2b	35		p m os		0.78	0	2.8783	0.025	0.1749	0.0023	2605	22	81.8	0.00223	14	0.280958	17	−5.4	0.6		
44_2b	41	3	b m h		0.38	89	2.0282	0.017	0.1760	0.0023	2615	22	99.4	0.00293	20	0.281006	18	−3.5	0.6	6.46	0.37
43_2b	45		p m os		0.52	41	2.0034	0.017	0.1781	0.0021	2635	20	99.5	0.00098	8	0.280950	18	−5.0	0.7		
42_2b	47	12	p m os		0.54	262	2.0430	0.017	0.1742	0.0021	2598	20	99.4	0.00142	9	0.280991	15	−4.4	0.5	7.79	0.41

(continued on next page)

Table 2 (*continued*)

Sample spot Lu-Hf	U-Pb [a]	O	Grain description [b]	α-Decay events/mg ($\times 10^{15}$ α/mg)	Th/U	^{204}(Hg + Pb)	$^{238}U/^{206}Pb$	1σ	$^{207}Pb/^{206}Pb$	1σ	Pb/Pb age (Ma)	1σ	Conc. (%)	$^{176}Lu/^{177}Hf$	2σ	$^{176}Hf/^{177}Hf_t$	2σ	ε_{Hft}	2σ	$\delta^{18}O_{VSMOW}$ (‰)	2σ
47_2b	49	11	p m os		0.61	0	2.5936	0.021	0.1775	0.0020	2630	19	86.7	0.00106	6	0.280988	17	−3.8	0.6	7.29	0.37
46_2b	60	9	p m h		0.64	0	6.5574	0.055	0.1248	0.0016	2026	22	57.1	0.00307	19	0.281070	21	−14.9	0.8	2.50	0.34
50_2b	64		p m os		0.70	372	2.8111	0.026	0.1771	0.0033	2625	30	82.6	0.00095	6	0.280982	19	−4.1	0.7		
48_2b	69	10	p e os		0.44	0	2.4799	0.020	0.1707	0.0020	2565	20	90.7	0.00150	10	0.281008	17	−4.6	0.6	6.02	0.36
51_2b	70		p e os		0.63	31	2.9303	0.024	0.1639	0.0020	2497	20	83.9	0.00069	4	0.280967	23	−7.6	0.8		
52_2b	78	6	b m os		0.65	40	2.0243	0.017	0.1782	0.0023	2636	21	99.0	0.00084	5	0.280974	19	−4.1	0.7	4.50	0.33
53_2b	78	8	b m os		0.65	40	2.0243	0.017	0.1782	0.0023	2636	21	99.0	0.00095	6	0.281002	16	−3.1	0.6	3.87	0.27
54_2b	80	5	p e os		0.27	785	5.5334	0.048	0.1843	0.0029	2692	26	36.9	0.00109	7	0.280968	16	−3.0	0.6	5.87	0.42
55_2b	81		p e os		0.83	28	2.0064	0.017	0.1798	0.0023	2651	21	99.1	0.00151	10	0.280954	17	−4.5	0.6		
MR257A																					
22	22		eq m os	2.33	0.46	37	1.9011	0.015	0.1860	0.0019	2707	16	100.4	0.00071	4	0.280967	33	−2.7	1.2		
34	34		p m os	3.40	0.67	40	1.9156	0.014	0.1874	0.0018	2719	16	99.8	0.00087	6	0.280990	33	−1.6	1.2		
37	37		p m os	3.41	0.37	95	1.9304	0.016	0.1895	0.0017	2738	15	99.0	0.00082	5	0.280989	29	−1.2	1.0		
42	42		p m os	1.39	0.40	30	1.9217	0.017	0.1882	0.0021	2727	18	99.5	0.00057	5	0.280934	22	−3.4	0.8		
48	48		eq m os	2.19	0.39	52	1.9057	0.017	0.1876	0.0022	2721	19	100.0	0.00060	4	0.280945	27	−3.2	1.0		
51	51		p m os	1.54	0.35	39	1.9273	0.015	0.1878	0.0017	2723	15	99.4	0.00058	4	0.280953	26	−2.8	0.9		
54	54		p m os	1.64	0.38	25	1.9204	0.015	0.1870	0.0017	2716	15	99.7	0.00064	4	0.280929	28	−3.9	1.0		
55	55		eq m os	3.08	0.32	71	1.9088	0.017	0.1879	0.0019	2724	17	99.8	0.00054	3	0.280935	33	−3.5	1.2		
60	60		f m os	0.78	0.57	30	1.9359	0.016	0.1877	0.0019	2722	17	99.2	0.00087	5	0.280948	37	−3.1	1.3		
61	61		eq m os	2.32	0.32	40	1.9107	0.015	0.1875	0.0018	2720	15	99.9	0.00093	10	0.280968	32	−2.4	1.1		
62	62		p m os	3.00	0.42	78	1.9206	0.016	0.1870	0.0018	2716	16	99.7	0.00153	15	0.280963	24	−2.7	0.9		
64	64		p m os	4.32	0.45	54	1.9046	0.018	0.1875	0.0023	2720	20	100.0	0.00080	7	0.280957	28	−2.8	1.0		
66	66		p m os	2.24	0.27	109	1.9410	0.017	0.1882	0.0024	2726	21	99.0	0.00037	3	0.280976	27	−1.9	0.9		

[a] Numbers in italic refer to geochronological data published by Farina et al. (2015).

[b] Grain description: Habit: p - prismatic, f - fragment, eq - equant, b - blocky, ov - oval, an - anhedral; Analysis site: c - core, m - middle, e - edge; Zonation: os - oscillatory, h - homogeneous, rx - recrystallized.

Table 3
Summary of ages and isotopic compositions for samples analysed in this study.
Data are from Farina et al. (2015), Lana et al. (2013), and Romano et al. (2013).

Sample	UTM Lat	UTM Long	Classification[a]	Crystallisation age ± 2σ (Ma)[b]	Type[c]	N_1[d]	Inherited (Ma)	Metamorphic (Ma)	Average $^{176}Hf/^{177}Hf_{int}$ ± 2σ[e]	Average εHf_{int} ± 2SD[e]	N_2[f]	$\delta^{18}O$ ± 2SD[g]	Published age	Reference[h]
Bação complex														
FQ1	643228	7746959	Kfs-rich	2711 ± 3	conc	6			0.280989 ± 23	−1.8 ± 2.3	22 of 22	5.5 ± 2.1		[1] - This study
FQ2	644685	7749318	Banded	2868 ± 10	wm	13		2705 ± 18	0.281009 ± 24	2.6 ± 2.1	19 of 19	3.9 ± 1.6		[1] - This study
FQ5 (=MR11)	625597	7762152	Plag-rich	**2761 ± 11**	wm	9	1 core at 3292		0.281002 ± 22	−0.2 ± 1.8	18 of 18		2744 ± 10	[2] - This study
FQ6 (=D12)	625629	7762157	Kfs-bearing	**2779 ± 4**	conc	3	2891 ± 3	2705 ± 7	0.280970 ± 23	−0.9 ± 2.2	3 of 3		2764 ± 10	[3] - This study
FQ8	628585	7760332	Kfs-bearing	–	wm		2770 ± 42	2612 ± 10						This study
FQ11	628157	7751740	Plag-rich	2790 ± 3	conc	6	2905 ± 17	2719 ± 14	0.281019 ± 18	1.1 ± 2.0	5 of 5			[1]
FQ13	628731	7748442	Banded	2790 ± 3	conc	17	ca. 2900		0.281030 ± 26	1.5 ± 1.2	12 of 14			[1]
FQ14	637895	7750487	Migmatite	**2692 ± 4**	conc	6	From ca. 2930 to ca. 3470		0.281020 ± 29	−1.2 ± 2.3	4 of 4			This study
FQ17	625643	7755180	Banded	2778 ± 2	conc	8	2862 ± 2	2732 ± 10	0.280982 ± 21	−0.2 ± 1.3	8 of 9	5.4 ± 1.6		[1] - This study
FQ20 (=D07A)	620091	7749557	Banded	–	conc		2 cores at 2829 and 2772	2723 ± 3					2918 ± 10	[3] - This study
FQ23	644680	7749530	Banded	2898 ± 12	wm	8		2783 ± 18	0.280977 ± 21	2.1 ± 3.3	8 of 8			[1]
Bonfim complex														
FQ29	603409	7765331	Plag-rich	2773 ± 2	conc	10			0.280910 ± 18	−3.2 ± 1.3	42 of 42	4.9 ± 1.8		[1] - This study
FQ37	603293	7759954	Amphibolite	2719 ± 14	wm	9	2879 ± 14		0.280956 ± 24	−2.8 ± 2.9	9 of 9			[1]
FQ40	593263	7767241	Kfs-bearing	2854 ± 18	ui	4		2670 ± 15	0.280871 ± 20	−2.7 ± 1.1	4 of 4			[1]
FQ41	595299	7765480	Banded	2852 ± 16	wm	5			0.280898 ± 20	−1.8 ± 0.9	17 of 17			[1]
FQ51	603378	7741084	Plag-rich	2678 ± 10	wm	14			0.281026 ± 22	−1.3 ± 1.3	28 of 28			[1]
FQ52	582109	7761295	Banded	–	wm			2727 ± 11				4.6 ± 2.1		[1] - This study
MR31A	594650	7775356		**2716 ± 14**	wm	13			0.280958 ± 28	−2.8 ± 0.7	12 of 12		2700 ± 8	[2] - This study
MR22A (=FQ28)	602440	7769392	Kfs-rich	**2715 ± 2**	conc	22	3 cores at 3515, 3141 and 2835		0.280930 ± 26	−3.8 ± 1.8	7 of 7		2730 ± 8	[2] - This study
MR70G	602011	7727899		**2716 ± 6**	wm	33			0.280948 ± 28	−3.2 ± 1.5	20 of 20		2723 ± 7	[2] - This study
MR87A (=FQ50)	608581	7738759	Kfs-rich	**2646 ± 9**	wm	22	2734 ± 8		0.280960 ± 26	−4.4 ± 1.6	21 of 21		2613 ± 6	[2] - This study
MR14A (=FQ32)	608654	7756333	Kfs-rich	**2715 ± 3**	conc	9			0.280955 ± 28	−3.0 ± 1.6	7 of 7		2730 ± 7	[2] - This study
Belo Horizonte complex														
FQ60	548149	7801529	Plag-rich	2728 ± 16	wm	6	2786 ± 29		0.280962 ± 21	−2.4 ± 2.0	17 of 18	4.6 ± 2.9		[1] - This study
FQ65 (=MR259A)	537885	7835546	Plag-rich	–	wm			2645 ± 8						[1]
FQ70	579027	7790240	Banded	–	conc			2713 ± 3						[1]
FQ74	555202	7842055	Kfs-rich	–	wm			2638 ± 14				5.4 ± 3.2		[1] - This study
FQ81	642637	7796689		–	conc			2671 ± 10						This study
MR257A	537893	7835513		**2723 ± 8**	wm	18			0.280958 ± 30	−2.7 ± 1.4	13 of 13		2706 ± 7	[2] - This study
MR259A	539550	7834072	Plag-rich	**2721 ± 9**	wm	15			0.280949 ± 29	−3.0 ± 2.2	9 of 9		2722 ± 7	[2] - This study
MR51A	621958	7803440		**2708 ± 10**	wm	10			0.280950 ± 27	−3.3 ± 1.3	18 of 19		2700 ± 8	[2] - This study

[a] According to the classification of Farina et al. (2015).
[b] Intrusion age. Ages in bold indicate ages obtained during this study, regular font indicates ages already published by Farina et al. (2015).
[c] Type: conc - concordia, wm - weighted mean, ui - upper intercept.
[d] Number of individual U-Pb spots used in age calculations.
[e] $^{176}Hf/^{177}Hf_{int}$ and εHf_{int} calculated using the intrusion age of each sample (excluding inherited cores or metamorphic domains).
[f] Number of individual Lu-Hf spots used in the calculation of the average $^{176}Hf/^{177}Hf_{int}$ and εHf_{int}.
[g] $\delta^{18}O$ calculated using the intrusion age of each sample, except for FQ52 and FQ74 where we used the metamorphic age.
[h] References: [1] - Farina et al. (2015), [2] - Romano et al. (2013), [3] - Lana et al. (2013).

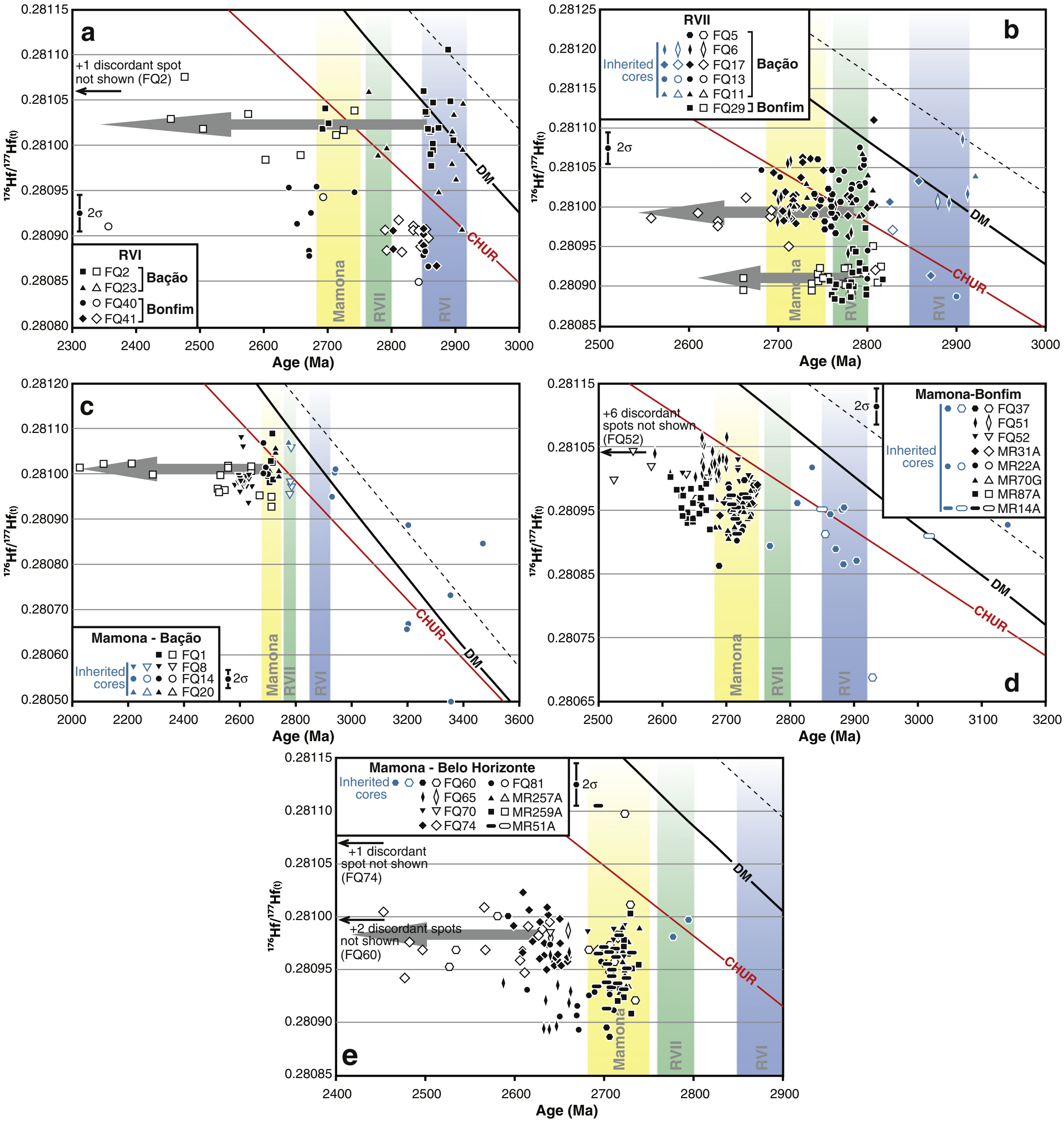

Fig. 2. $^{176}Hf/^{177}Hf_t$ vs. apparent $^{207}Pb/^{206}Pb$ age diagrams for each magmatic event described in Section 2. Filled symbols represent analyses with >95% concordance, open symbols are analyses with <95% concordance. Grey horizontal arrows indicate Pb-loss trends within individual samples. The Depleted Mantle (DM) (full line) composition is from Guitreau (2012), while the dashed line represents the most radiogenic DM composition from Blichert-Toft and Puchtel (2010) (see text for explanation).

falling in the compositional field of Archean "low δ^{18}O zircon" (2–4‰) from Hiess et al. (2011) (Fig. 3). Low δ^{18}O values in zircon indicate that the grains either crystallized from, or diffusively exchanged O with a low δ^{18}O melt or fluid (e.g. Bindeman et al., 2008; Gilliam and Valley, 1997; Hiess et al., 2011; Valley et al., 2005). Two gneisses from the Bação complex contain metamorphic rims surrounding oscillatory zoned grain interiors interpreted as crystallization features. For both samples, the δ^{18}O values obtained for the rims are identical to those obtained for the magmatic domains, indicating either that there was no change in O isotope between the magmatic and metamorphic magmas/fluids, or that the O isotope system was not disturbed during the metamorphic event. Additionally, the two following trends can be observed within this dataset: (1) the δ^{18}O values for individual samples increase with time from an average of 3.9 ± 0.2‰ at 2868 Ma (FQ2) to 5.4 ± 0.4‰ at 2638 Ma (FQ74), in concert with (2) a notable increase in the range of δ^{18}O composition per sample, from ±1.6‰ for FQ2 to ±3.2‰ for FQ74 (2SD) (Fig. 3).

5. Discussion

5.1. Origin of the Meso- and Neoarchean granitoids

5.1.1. Interpretation of the Hf vs. time arrays

The crustal evolution of the three basement complexes of the SSFC will be treated separately in the following discussion. The linear Hf array (Fig. 4), the presence in RVII rocks of RVI inherited zircon cores,

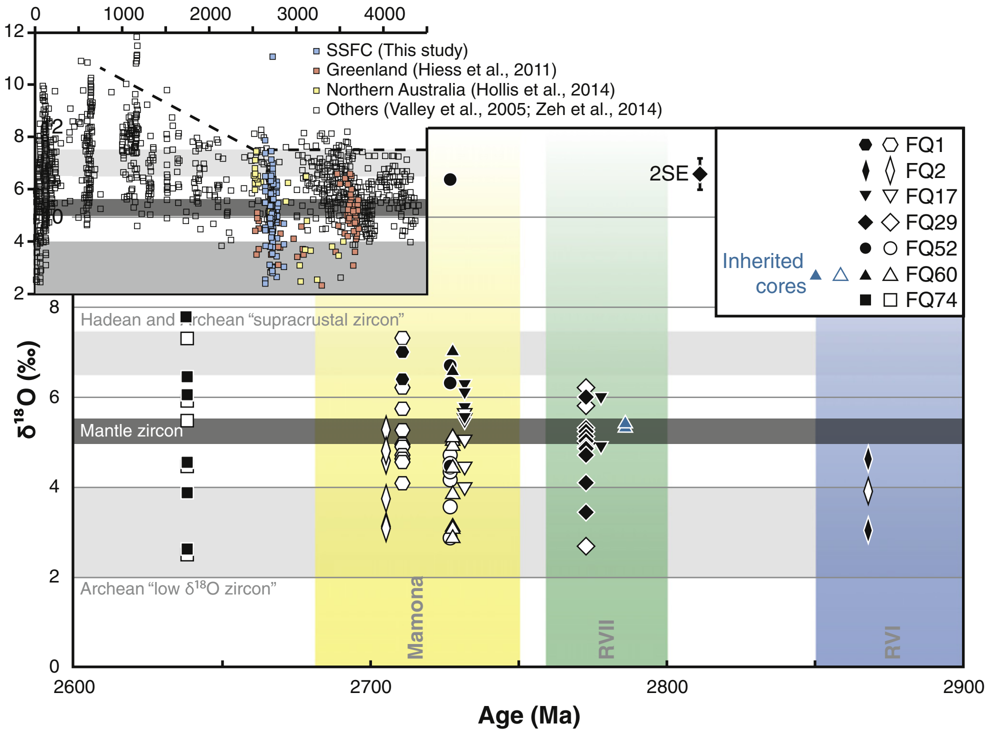

Fig. 3. $\delta^{18}O$ vs. intrusion age diagram. Filled symbols represent O analyses on zircons with >90% concordance, open symbols are zircons with <90% concordance. Fields for Hadean and Archean "supracrustal zircon" and Archean "low $\delta^{18}O$ zircon" are from Cavosie et al. (2005) and Hiess et al. (2011) respectively. The "mantle zircon" field is 5.3 ± 0.3‰ as defined in Valley et al. (1998). Inset: $\delta^{18}O$ values of dated zircons from this study, plotted against a compilation from Valley et al. (2005) and Zeh et al. (2014). Zircons from the Greenland (Hiess et al., 2011) and Northern Australian (Hollis et al., 2014) cratons where low $\delta^{18}O$ values were reported are plotted for comparison.

as well as the presence in RVI and RVII rocks of metamorphic rims formed during the Mamona event indicate that the Bação complex underwent progressive crustal reworking throughout the Neoarchean time. These lines of evidence can be correlated with (1) the close relationships observed in the field between gneisses and small granitic intrusions (e.g. xenoliths of gneisses within the granites), and (2) the geochemistry of the gneisses suggesting a derivation from mixing between a crustal component derived by melting of an older TTG and a more mafic juvenile end-member (Farina et al., 2015). Indeed, these authors observed that these rocks have intermediate compositions between those of "true" TTGs and those of experimental melts derived from fluid-absent partial melting of TTGs. The RVI gneisses in the Bação complex were mostly generated through melting of a mafic crust, with only a limited proportion of reworked felsic crust. This is supported by: (1) overall geochemical compositions that are comparable to those of "true" TTGs, (2) the scarcity of inherited zircons, and (3) superchondritic Hf isotope compositions. Patchett and Arndt (1986) demonstrated that because of its higher Nd content compared to that of the mantle, the amount of continental crust needed to reduce the εNd composition of a Proterozoic granite from +5 down to 0 is small (<10%). Although this example was made using Nd isotopes, the same logic applies to the Hf system. Therefore we suggest that the volume of reworked component involved in the generation of the RVI gneisses from the Bação complex was probably <10%.

It is interesting to note the large range in initial Hf isotopic compositions displayed by the RVI gneisses (εHf between 0.0 and +6.5). This is rather uncommon in typical I-type granitoids, and could be explained in several ways, which include incomplete mixing between two isotopically different magmas (in this case, a crustal component and a more juvenile, mafic one), or as inherited from the source, as a result from incomplete homogenization of the magma during dissolution and crystallization of isotopically heterogeneous zircons (Farina et al., 2014; Villaros et al., 2012). The subsequent reworking of this crust during RVII, with some minor contribution from juvenile material produced granitoid magmas with lower (superchondritic to chondritic) $^{176}Hf/^{177}Hf$ isotope ratios and compositions that are "transitional" between those of a TTG-like end-member and a high-K one. Further reworking of this "transitional" crust during the Mamona event generated high-K granitoids with subchondritic Hf isotope compositions. One gneiss sample from the Bação complex (FQ14) displaying migmatitic structures with garnet-rich leucosomes provides evidence of inheritance of distinctly older crust (concordant zircons of up to ~3.47 Ga). The occurrence of inherited cores with ages clustering between 2933 and 3465 Ma suggest that the protolith for FQ14 was a (meta)sedimentary rock that underwent partial melting during the Mamona event.

In the Bonfim complex, the RVI event is represented by two gneiss samples (Alberto Flores gneiss), with low $\varepsilon Hf_t = -1$ to -4. Samples from the Alberto Flores gneiss show highly variable compositions which differ from those of "true TTGs" (e.g. higher Si, K, Rb and lower Al contents). This suggests the involvement of reworked continental crust in their petrogenesis (Farina et al., 2015), a hypothesis which can be reconciled with their subchondritic Hf isotope data. During RVII, the Bonfim complex is intruded in the east by the Samambaia tonalite. This magma has an evolved Hf isotope composition ($\varepsilon Hf_t = -2$ to -4) that falls within the εHf array defined for the Bonfim complex. However, a derivation from an older felsic crust formed during RVI for example can be ruled out, as it cannot account for the intermediate compositions of the Samabaia tonalite (i.e. SiO_2 ranging from 64 to 72 wt.%) (Carneiro, 1992; Farina et al., 2015). Instead, its enriched Hf isotopic signature probably originates from assimilation of older felsic crust by a more mafic magma. The Mamona event is mostly represented by large high-K batholiths emplaced in the eastern and northern borders of the dome, namely the Mamona and Souza Noschese batholiths. These granites all have subchondritic εHf_t values ranging from −1 to −6 that plot on an array defined by the gneisses of the Bonfim complex (Array 2, Fig. 4). This array suggests that high-K granitoids formed by reworking of the previously formed crust. However,

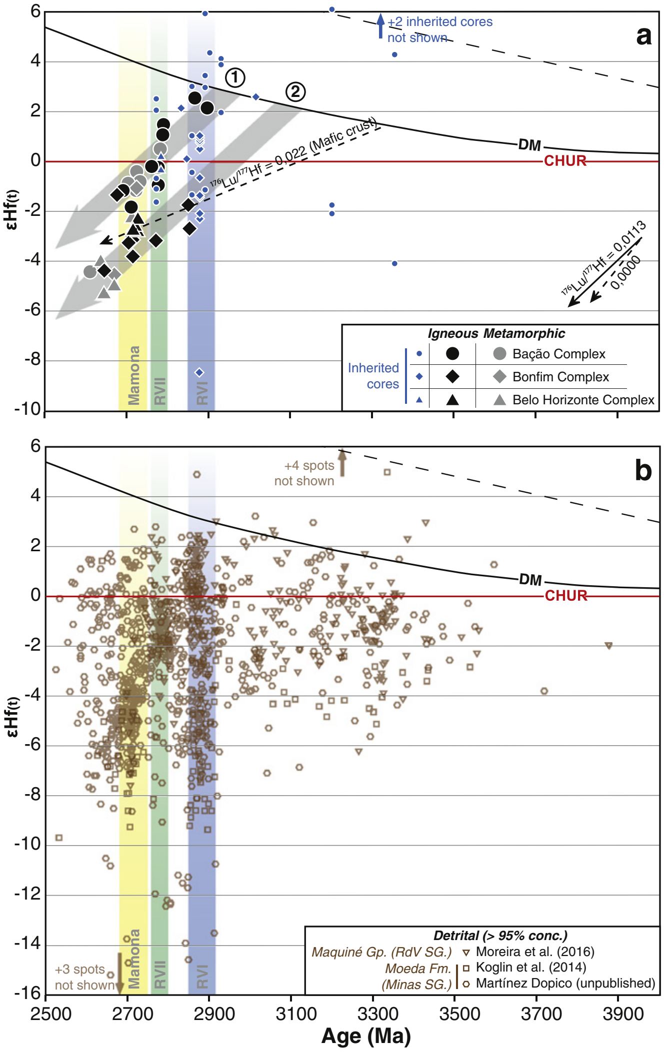

Fig. 4. εHf_t vs. age diagrams for: (a) igneous and metamorphic zircons (this study). The diagonal grey arrows indicate crustal evolution trends derived from the Hf data of this study, using an average $^{176}Lu/^{177}Hf$ of 0.0113 for the average continental crust. The arrays 1 and 2 are fitted through the average compositions of the granitoids and gneisses of the (1) Bação and (2) Bonfim + Belo Horizonte complexes respectively, indicating that the complexes evolved as different terranes or portions of the crust, and (b) detrital zircons (data from Koglin et al., 2014; Moreira et al., 2016; Martínez Dopico, unpublished) of the SSFC. The Depleted Mantle (DM) evolution is as in Fig. 2.

the K and LILE content of these rocks is too high to be explained by a derivation from partial melting of the orthogneisses. Farina et al. (2015) therefore argued that the large high-K batholiths emplaced during the Mamona event require a source that is more enriched in K and LILE, and more fertile than the average continental (medium-K) crust present in the SSFC at the time, suggesting their derivation by melting of metasedimentary protoliths such as metagreywackes.

In the Belo Horizonte complex, the Mamona event is marked by the coeval intrusion of granitoids with very different field and geochemical features: (1) in the east, two voluminous batholiths (Pequi and Florestal) are characterized, as opposed to those emplaced in the Bonfim complex, by homogeneous sodic compositions presenting some similarities with TTGs (e.g. typically high Al_2O_3, CaO, Na_2O, Sr, LREE and low K_2O, Rb, Y, HREE), and (2) smaller granitoid domains/dikes and leucogranites, showing a wider range of more enriched compositions. The petrology and geochemistry of the former suggest a derivation from a hydrous mafic rock. Assuming this is the case, their low Hf isotope signatures can be explained in two ways: (1) partial melting of an old mafic crust. This however implies that this mafic precursor was extracted from the depleted mantle long before remelting to produce these magmas. In particular, considering an average $^{176}Lu/^{177}Hf = 0.022$ for a mafic crust (Nebel et al., 2007), this corresponds to >600 m.y. of crustal residence time (Fig. 4), or (2) partial melting of a mafic crust but with assimilated portions of much older crust.

The existence of several Archean basement complexes with distinct εHf vs. time arrays (Fig. 4) suggests that these terranes underwent partly/largely different histories. In this scenario, it is possible to imagine that the basement presently exposed in the SSFC consists of a collage of different micro-continental blocks amalgamated during a late collisional stage.

5.1.2. Secular trend: from sodic to potassic magmatism

We have combined the Hf isotope data presented here with geochemical results obtained by Farina et al. (2015) for sixteen igneous samples. The results are presented in Fig. 5, where εHf_t for each sample is plotted against some key geochemical features (K_2O/Na_2O, Th and Sr/Y), representative of the trends observed here. Magmas produced during RVI share similar features with TTGs, such as high Na_2O, $(La/Yb)_N$, low K_2O, Th, U contents, and high Sr/Y, usually interpreted to reflect the depth at which those TTG magmas are produced. However, it is important to note that small differences do occur between "true" TTG magmas and those of the SSFC (e.g. lower Sr/Y, Fig. 5). During RVII, the magmas display a wider range of more evolved compositions (e.g. K_2O/Na_2O up to 1, Th up to 20 ppm), however still overlapping the compositional field of TTGs. The magmas produced during the Mamona event all have subchondritic Hf isotope signatures but heterogeneous trace element compositions. In particular, we observe systematic differences between magmas forming large batholiths in the Belo Horizonte complex which are similar to TTGs, and those emplaced as the large batholiths of the Bonfim complex, which present the highest K/Na and lowest Sr/Y compositions of this dataset. Between these two end-members, we observe a range of (much less voluminous) magmas with intermediate compositions and different petrological features (from sodic Plag-rich granites to Kfs-rich granitoids, Farina et al., 2015).

Overall, the most striking feature is the relatively continuous evolution trend with decreasing age (and decreasing εHf_t), from compositions close to those of TTGs to more enriched granitoids. In particular, we observe a progressive enrichment in High Field Strength Elements (HFSE) with time (e.g. Th from 6 to 30 ppm). These trends cannot be explained as a result of different degrees of fractionation from a similar source, as these magmas almost all have very similar high SiO_2 contents (>70 wt.%). HFSE are highly immobile elements, and are usually considered as good tracers of source enrichment. We infer that these trends reflect crustal maturation and differentiation via progressive reworking at shallower crustal levels. In addition, it is important to note that the wide range of geochemical compositions characteristic of Mamona granitoids mirrors the diversity of processes and sources involved in the generation of these magmas, which cannot be appreciated using Hf isotopes alone. The trends documented here are not exclusive to the SSFC, and similar ones are well described in the Yilgarn and Pilbara cratons of Western Australia for example (Griffin et al., 2004; Ivanic et al., 2012). There, nearly continuous crustal melting over a protracted period of time has recorded a transition from sodic (TTG) to potassic magmatism, which is interpreted to reflect a similar scenario of progressive reworking.

5.1.3. Insights from O isotopes

5.1.3.1. Do these $\delta^{18}O$ values represent primary magmatic features?. The interpretation of O isotope data depends critically on whether the measured O isotope compositions reflect that of the magmas from which the zircons crystallized, or if they are product of secondary alteration processes and isotopic exchange. In CL images, zircons generally display euhedral habits and oscillatory growth zonation. Th/U are

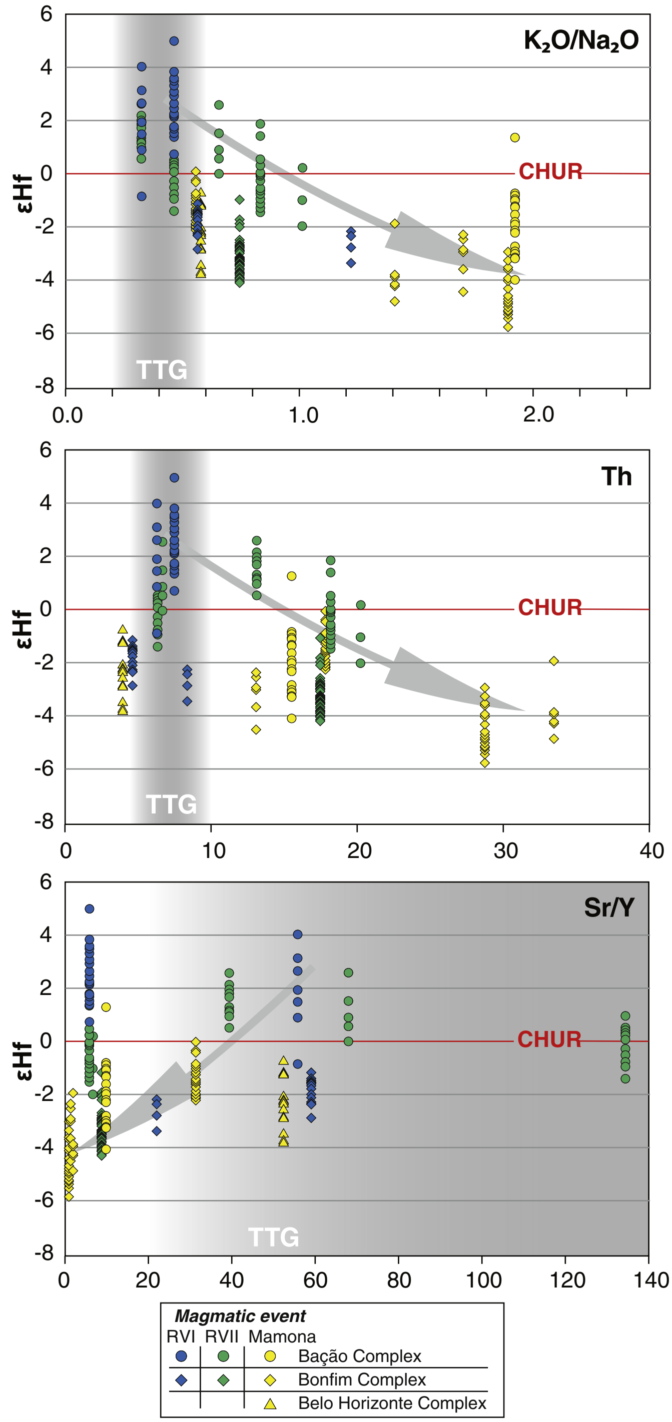

Fig. 5. Plots of εHf_t vs. geochemical parameters, showing general trends of enrichment with decreasing age and εHf_t of the magmas (grey arrows). The grey fields represent TTG compositional fields from Moyen (2011).

between 0.02 and 0.8, and only 7 out of 75 spots analysed have Th/U < 0.1. However, a significant amount of zircons have low levels of U-Pb concordance (ca. 30% of zircons have concordance < 80%), which can cast doubts on the interpretation of the isotope compositions as primary values. Valley et al. (1994) observed that Pb-loss (indicated by higher levels of discordance) is always associated with resetting of O isotope ratios, shifting $\delta^{18}O$ values up to 2‰ lower than their primary values. However, these authors observed that there is no apparent proportional relationship between the degree of concordance and the shift in O isotope ratio (Valley et al., 1994, their Fig. 4). In other words, elevated levels of discordance are not necessarily coupled with highly disturbed O isotope ratios. For most samples in this dataset, no correlation is observed between $\delta^{18}O$ and Th/U, $^{204}(Hg + Pb)$ or the degree of concordance (%), which suggests that $\delta^{18}O$ values and radiation doses U-Pb systematics cannot be directly associated (Fig. 6). Overall, we argue that most of the zircons from the São Francisco craton analysed in this study have preserved their primary isotopic signatures and that these reflect that of the magmas they crystallized from.

We note however that two samples (FQ52 and FQ60) show a slight positive correlation between $\delta^{18}O$ and the level of concordance of the zircons (Fig. 4c). Zircons from FQ52 sometimes display faint oscillatory zoning disrupted inwards from the grain boundary by recrystallized domains. The edges of the grains commonly contain inclusions and/or fractures suggesting that the zircons were affected by fluid-dominated recrystallization (as described by Hoskin and Black, 2000), probably during the metamorphic event dated by this sample at 2727 ± 11 Ma. By contrast, the zircons analysed from FQ60 are mostly euhedral and display clear oscillatory zoning patterns, with no sign of pervasive alteration in CL or BSE images. In this case, it is not clear what process caused the Pb-loss and the disruption of the Hf system. Together, this suggests that FQ52 and maybe FQ60 underwent some degree of post-magmatic

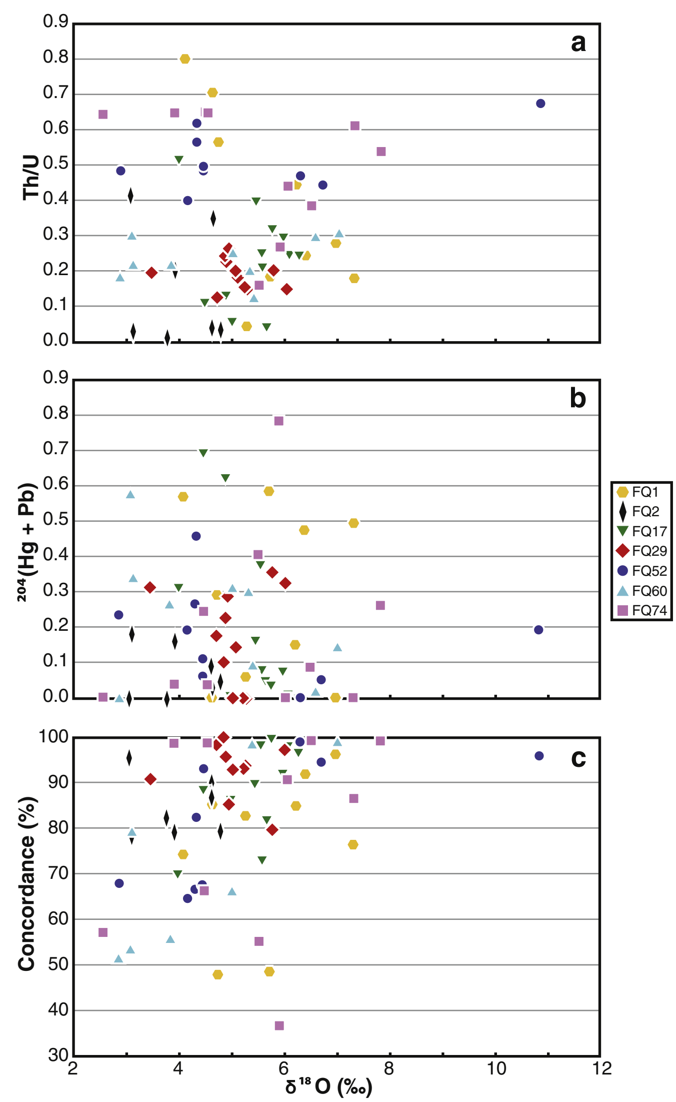

Fig. 6. $\delta^{18}O$ vs. U-Th-Pb systematics diagrams. The lack of apparent correlations indicates that the $\delta^{18}O$ values are not products of secondary alteration and can instead be considered as primary features (see text).

alteration causing a shift towards some of the low $\delta^{18}O$ values observed in the most discordant zircons.

5.1.3.2. Secular trend of increasing $\delta^{18}O$ values: evidence for supracrustal reworking. If they can fingerprint involvement of crustal material, Hf isotopes alone do not allow determining whether contamination occurred via (1) source mixing, whereby the recycling of subducted materials into the source reservoir influences the isotopic signature of the resulting magmas, or (2) crustal contamination, that is contamination of the magma during ascent and/or emplacement by interaction (assimilation) with the crust it intrudes. In modern arcs, stable (e.g. O) and radiogenic (e.g. Nd, Hf, Sr) isotopes have been used widely to discriminate between these contamination processes (Appleby et al., 2010; Kemp et al., 2006; Peck et al., 2000).

The first trend in the O isotope data is the steadily increasing maximum $\delta^{18}O$ throughout the Neoarchean, from ~5.3‰ at 2.87 Ga to ~7.8‰ at 2.64 Ga (Fig. 3). This follows the general trend defined by a global O isotope dataset (Roberts and Spencer, 2014; Valley et al., 2005). In the global dataset, this secular rise of magmatic O isotope ratios is explained by a combination of modifications in sediment composition, availability, weathering and burial, originating from a change in tectonic styles at the Archean-Proterozoic boundary (Valley et al., 2005). In this study, the appearance of high $\delta^{18}O(Zrc)$ (>6.5‰) in rocks at ~2.7 Ga indicates reworking of supracrustal lithologies during the last Mamona event, this either being sedimentary rocks (10 to 40‰) or altered volcanics (20‰) (Eiler, 2001). Archean sediments, dominated by greenstone belt assemblages made of volcaniclastics, pyroclastics and less mature sediments record lower $\delta^{18}O(WR)$ ratios compared to their modern counterparts (Longstaffe and Schwarcz, 1977; Veizer and Mackenzie, 2003). Using an average of 15‰ for Archean sediments (average of Archean sandstones and shales from Valley et al., 2005), we estimate that 10–20% of sedimentary contaminant would be required to increase the $\delta^{18}O$ of a normal igneous rock and zircons by 1–2‰, the amount required to reach the range of $\delta^{18}O$ measured here. The question remains to determine whether these high $\delta^{18}O$ result from upper-crustal contamination or via direct sediment reworking. While we cannot completely rule out the possibility that these high $\delta^{18}O(Zrc)$ values originate from assimilation of upper-crustal lithologies, the involvement of metasediments is in agreement with the model proposed earlier for the petrogenesis of these rocks.

5.1.3.3. The origin of the low $\delta^{18}O$ magmas. About 50% of all O isotope analyses have values below the range of mantle zircon compositions (<5.3 ± 0.3‰, Fig. 3). Low $\delta^{18}O$ values indicate that the zircons either crystallized from, or exchanged O via diffusion with a low $\delta^{18}O$ melt or fluid. The only low $\delta^{18}O$ materials are meteoric and seawater and materials that have undergone alteration with these fluids at high temperatures. Eiler (2001) indicated that the lower gabbroic portion of oceanic crust preserves a low $\delta^{18}O(WR)$ (0–5‰) acquired during high-temperature interaction with percolating water at the ridge. We propose two different possible interpretations to account for the systematic presence of low $\delta^{18}O$ zircons in all three magmatic events.

The first model stems from the fact that all these rocks derived from a diversity of rather well-characterized sources and processes (Farina et al., 2015; this study), and that perhaps a single unique mechanism is unlikely to account for the low $\delta^{18}O$ values observed in all of them. We therefore consider them separately. The magmas emplaced during the RVI event (FQ2) have $\delta^{18}O$ values that range from ~3 to 5‰. This rock is inferred to result from mixing between a juvenile material and a TTG-derived melt (Farina et al., 2015). The superchondritic εHf_t values displayed by the zircons in FQ2 indicates only a minor component of evolved crust within this magma (<10%). These first-order observations suggest that >90% of the source of this rock was a juvenile rock, and that it had to account for the O isotope compositions observed. The low $\delta^{18}O(Zrc)$ values of FQ2 can be explained as a result of partial melting of a lower and relatively young $\delta^{18}O$-depleted gabbroic oceanic crust. The resulting melts will then mix with a small proportion of a continental crustal component, possibly originating by local wall-rock melting of the surrounding TTG crust. The RVII magmatic zircon population, documented by sample FQ29 and a few inherited cores displaying mantle-like values, is centred around mantle-like $\delta^{18}O$ values. It is worth noting that zircons from FQ29 display a small spread towards low $\delta^{18}O$ values, with two grains plotting in the field of "low $\delta^{18}O$ zircons", and relatively clustered evolved Hf compositions ($\varepsilon Hf_t = -1.0$ to -4.2). Derivation of these rocks by reworking of RVI continental crust to explain its evolved Hf composition, as may be suggested by the Hf linear array, can be ruled out on the basis that this existing crust had SiO_2 contents greater than 70 wt.% and was therefore incapable of giving rise to some of the more mafic compositions (SiO_2 = 65–70 wt.%) recorded in the Samambaia samples (Carneiro, 1992; Farina et al., 2015). Moreover, field and geochemical observations suggest the involvement of a mantle source component for the Samambaia tonalite (Farina et al., in prep.), which is in agreement with the observed mantle-like $\delta^{18}O$ compositions. In this context, the unradiogenic Hf isotope composition of sample FQ29 could be explained either by assimilation or source contamination by an evolved and slightly $\delta^{18}O$-depleted crustal component. It is interesting to speculate on the origin of the low $\delta^{18}O$ magmatic zircons observed in rocks from the Mamona event. Samples emplaced at that time all record $\delta^{18}O$ values above those of the mantle, attributed to the reworking of $\delta^{18}O$-enriched metasediments. However, this process does not account for the $\delta^{18}O$-depleted zircons. Firstly, we should address the question of the nature of the fluid responsible for the $\delta^{18}O$-depleted compositions. If the O composition of seawater is assumed to be constant and equivalent to its present-day value ($\delta^{18}O$ ~0‰, Gregory, 1991), then high-temperature exchange with seawater would require very large volumes of seawater to explain the low $\delta^{18}O$ observed. Instead, meteoric fluids have compositions between 0 and −55‰ (Bindeman, 2011), a range that is more plausible to produce the $\delta^{18}O$-depleted compositions. In recent magmatic systems reporting low $\delta^{18}O$ magmas, the latter are interpreted to originate within shallow sub-volcanic magma chambers where assimilation of hydrothermally altered wall rock has occurred (e.g. Bindeman and Valley, 2001; Monani and Valley, 2001; Wotzlaw et al., 2012). Where these low $\delta^{18}O$ zircons occur in the Archean, similar settings (shallow-level geothermal systems) have been proposed (Hiess et al., 2011; Hollis et al., 2014). In such environments, the emplacement of new granitoid magmas effectively drives groundwater into the crust through fracture networks where these meteoric fluids heterogeneously interact with wall rocks, lowering their O isotope compositions (Taylor, 1977). The isotopic heterogeneity observed in some samples (e.g. FQ74) is consistent with such an environment. These systems generally require that magmas are emplaced at relatively shallow levels, to have access to meteoric water. In general, low $\delta^{18}O$ values are scarce, particularly amongst Archean rocks (Valley et al., 2005), where they have only been reported in southwest Greenland (Hiess et al., 2011) and northern Australia (Hollis et al., 2014) (see inset in Fig. 3), testifying of either their rarity, or a lack of preservation of such materials. Therefore, this model may be hampered by the fact that it requires low $\delta^{18}O$ material to be generated at three consecutive times in the same area, which may be considered unlikely for this has not been documented elsewhere.

Alternatively, the systematic presence of these low $\delta^{18}O$ values could be interpreted as resulting from a single hydrothermal alteration event, producing a significant amount of $\delta^{18}O$-depleted material whose O isotope signature is then carried through the subsequent crustal reworking events. In this scenario, we propose that the source of the RVI gneisses, essentially a juvenile mafic rock, most probably oceanic crust, was contaminated by a significant amount of meteoric water during formation at a submarine rift zone, generating dynamic hydrothermal systems (see Eiler, 2001). Moreover, this is in agreement with the consensus that TTGs commonly derive from a partially hydrated mafic crust (e.g. Rapp and Watson, 1995). The systematic presence of these values in rocks from all three magmatic events highlights both the lack of efficient magma mixing, as well as the fact that reworking is not swamped by addition of new crust through the subsequent important magmatic events. In this hypothesis, the low $\delta^{18}O$ signatures act as an effective tracer for crustal reworking in the SSFC, much in agreement with the Hf isotope data.

Overall, although both models propose slightly different interpretations of these low $\delta^{18}O$ values, the data definitely indicates the interaction between meteoric water and crustal rocks at least once in the Mesoarchean and possibly also during the Neoarchean Mamona event in the SSFC. Given the proposed importance of oceanic crust in the formation of TTG magmas, it is perhaps surprising that low $\delta^{18}O$ TTGs have not been more commonly reported.

5.2. The growth of the continental crust in the SSFC

5.2.1. Archean depleted mantle evolution

Model ages are commonly used to produce estimates of crustal growth events (e.g. Bennett and DePaolo, 1987). This is based on the premise that model ages reflect the age of extraction from a depleted mantle reservoir, with zircon crystallization occurring only later on. Current models suggest that the depletion of the upper mantle from a chondritic reservoir started very early in Earth's history and was extrapolated more or less continuously, resulting in a linear $^{176}Hf/^{177}Hf$ array to reach its current composition, constrained by present-day MORB. Although some rocks show local evidence for early (Hadean) mantle depletion (e.g. suprachondritic εHf_t values recorded in Eoarchean rocks from West Greenland, Pilbara and Barberton, Amelin et al., 2000), there is little data supporting derivation of early continental crust from a long-term Hf-depleted mantle reservoir. In fact, zircons from felsic rocks with ages > 3.5 Ga from a number of Archean terranes have maximum Hf isotope compositions similar to chondritic values (Amelin et al., 2000; Kemp et al., 2009b; Lancaster et al., 2014, 2015; Naeraa et al., 2012; Satkoski et al., 2013; Zeh et al., 2009). Similarly in the SSFC, there is a striking lack of zircon data with superchondritic Hf compositions, particularly observed within the detrital record (Fig. 4b). Koglin et al. (2014) and Moreira et al. (2016) argued that the subchondritic εHf_t compositions of zircons from the SSFC reflect intense reworking episodes of the crust, starting as early as ~3.4–3.5 Ma. An alternative view would be that the zircon record does not necessarily reflect crustal reworking, but instead argues against the presence of a strongly depleted mantle beneath the continental crust. Using a compilation of ~13,000 Lu-Hf analyses on zircons, Guitreau (2012) proposed a model of evolution for the depleted mantle that fits the maximum Hf compositions of zircons through time. This model is defined by a period of only minor increase of εHf_t for the first 1 Gy, followed by a period from ~3.5 to ~2.5 Ga of enhanced differentiation of the depleted mantle, followed after ~2.5 Ga by a constant increase, although slightly less steep, until a present-day value of $\varepsilon Hf_{today} = +18$. This model corresponds broadly to the "two-stage" evolution model discussed by Zeh et al. (2009) (their Fig. 12). It implies that for the first half of the history of the Earth, the source of the continental crust is not as depleted as proposed in the more commonly used models (e.g. that of Blichert-Toft and Puchtel, 2010). Applied to the SSFC, the model of Guitreau (2012) fits exceptionally well with the detrital zircon data (Fig. 4b). In addition, this model reduces the crustal residence time of zircons > 2.9 Ga from an average of 400 down to 200 m.y. Different tectonic settings in the Archean – with higher radiogenic heat production resulting in a large number of small unstable microplates and more dynamic tectonics – are more easily reconciled with shorter crustal residence times. For the next section, we tentatively use this depleted mantle model from Guitreau (2012) to discuss the crustal evolution of the SSFC.

5.2.2. Crustal growth

In order to discuss continent formation, understanding the growth of the continental crust involves evaluating the ratio between new magmatic additions directly extracted from the mantle (juvenile) and ones that originate from remelting of older crust (reworking). The main challenge when trying to determine the distribution of crustal growth using detrital zircon is to correct for the data that represents crustal reworking in order to calculate a crustal generation curve. Temporal Hf isotopic trends have been used in several regional studies (i.e. Boekhout et al., 2013; Kemp et al., 2009a) in order to estimate the varying degrees of mantle input in the generation of granitic magmas. In this study, the regional magmatic evolution of the SSFC was explored using U-Pb and Lu-Hf data from detrital zircon from recent publications focused on the Neoarchean supracrustal successions of the Maquiné Group (Moreira et al., 2016) and Moeda Formation (Koglin et al., 2014; Martínez Dopico, unpublished). Modelling of the degree of juvenile growth was largely based on the calculation techniques applied by Belousova et al. (2010). Five zircons with $\varepsilon Hf_t > 2\ \varepsilon Hf_{DM}$ were rejected. In total, 1178 analyses were used for modelling. All the crustal T_{DM2} ages for these zircons were recalculated according to the depleted mantle evolution model of Guitreau (2012) for which we have graphically determined the equation for this age interval (4.0–2.5 Ga) (Fig. 7b). For all the other parameters (Lu decay constant, CHUR parameters and average $^{176}Lu/^{177}Hf$ of the crust), we have adopted the same values as indicated in the Analytical Techniques section of the Supplementary Material. The results of the modelling are summarised in Fig. 7.

The distribution of U-Pb detrital zircon ages along with an integral curve are plotted in Fig. 7a. The three major peaks observed at ca. 2.88, 2.79 and 2.72 Ga correspond to the RVI, RVII and Mamona events, respectively. Their presence reflects the good preservation of Neoarchean rocks in the SSFC. The existence of continental crust older than 2.9 Ga, although it is absent in the field, is evidenced by the Hf model ages of the detrital zircons. The dark blue line in Fig. 7a represents the cumulative curve of crustal model ages obtained for this dataset. It suggests that if the generation of new crust was predominant during the Paleoarchean, the importance of crustal reworking increased after 2.9 Ga. However, the Hf model ages on their own do not address the possibility that some of these zircons were produced from a mixture between a radiogenic component and an older crustal material with a lower Hf isotope composition. Payne et al. (2016) estimated that only a small proportion (14%) of Hf model ages actually provide a meaningful indicator of the timing of crustal growth, the rest of the model ages likely resulting from mixtures of melt derived from multiple mantle and crustal sources. Recent studies have used different methods in an attempt to remove this "mixed signal" and thereby accurately evaluate the proportion of juvenile material added to the crust at each step of its evolution (Belousova et al., 2010; Dhuime et al., 2012; Kemp et al., 2007). Zircons with juvenile Hf compositions are defined as falling in a range of $\pm 2\varepsilon$ units (or $\pm 0.75\%$) around the depleted mantle composition (Griffin et al., 2014). Using this simple definition, we have calculated the proportion of juvenile material produced at each time step, and obtained a cumulative curve (the green line in Fig. 7a) that is comparable to the one obtained from model ages, only slightly shifted towards older ages. Although debatable, these two simplistic approaches to estimate the growth of the continental crust in the SSFC indicate that most of it (ca. 95%) was already generated by 2.9 Ga (Fig. 7a), and that crustal reworking was dominating over net juvenile additions after 2.9 Ga. This conclusion is consistent with the geochemical data from granitoids of the SSFC, as discussed in Section 5.1.

Assuming that the generation of Archean granitoids involved interactions between juvenile and crustal sources, the average proportion of new crust through time can be estimated using two-components mixing calculations. This requires some assumptions to be made about the geochemical and isotopic compositions of the mantle and crustal end-members. Here we estimated the isotope composition of the crustal end-member from an "integral crust" calculation as described by Belousova et al. (2010). This integral crust is calculated so that the average signature of new crust is added successively to that of an

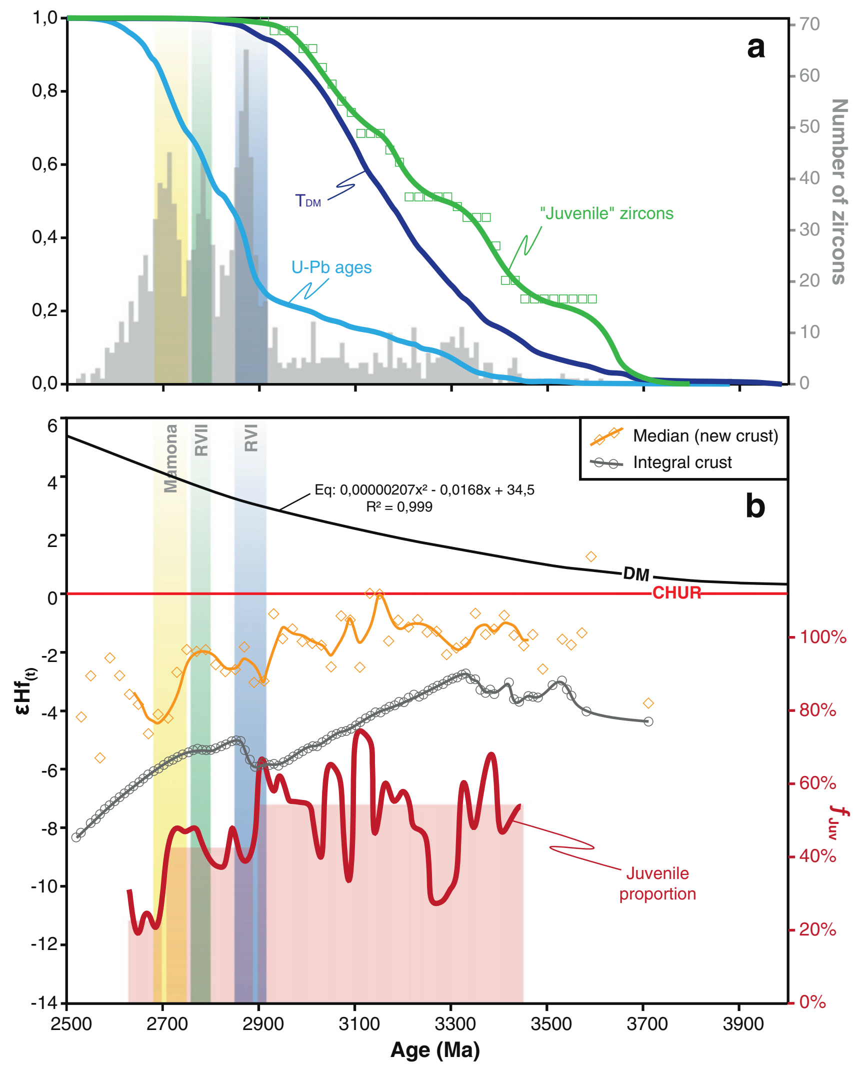

Fig. 7. (a) U-Pb age distribution for detrital zircons from the SSFC (grey bars; right scale) (data from Koglin et al., 2014; Moreira et al., 2016; Martínez Dopico, unpublished). Cumulative/integral curves of U-Pb ages (light blue) and of crustal T_{DM} ages (dark blue). The green line represents the integrated curve obtained from zircons defined as "juvenile" (with $\varepsilon Hf_t > 0.75 * \varepsilon Hf_{DM}$). (b) εHf_t vs. age diagram. The integral crust (grey line) is calculated following the method of Belousova et al. (2010). The proportion of juvenile component (red curve; right scale) is calculated in reference to the depleted mantle evolution from Guitreau (2012) and the integral crust (see text for explanation).

older and more evolved crust. This method is similar to the calculation of crustal model ages but with an interpolation projected forward instead of backwards. This provides a more realistic estimate for the average crustal composition than the use of a single value. Ages younger than 2.60 Ga and older than 3.45 Ga are largely under-represented in this dataset, therefore the calculations are statistically more subject to bias and the results obtained for these periods will not be discussed further. The juvenile fraction between a depleted mantle (that of Guitreau, 2012) and a crustal component (given by the integral curve) for bins of 20 Ma is calculated using mean Hf concentrations of 2.31 (Kelemen et al., 2003) and 4.0 ppm (average of TTG, Laurent et al., 2014) respectively. If we consider a truly depleted mantle with $[Hf]_{DM} = 0.157$ ppm (Workman and Hart, 2005), the calculated juvenile contribution shifts towards higher proportions. However as discussed in the previous section, the presence of a true depleted mantle beneath the SSFC in the Archean is questionable. Moreover, even if the quantitative proportions of juvenile material depend on this assumption, the temporal trends will remain the same. The results shown in Fig. 7b (red line) indicate that 20–70% of the melts generated at all times were juvenile. The following trends can be observed: (1) there is a general decrease in the juvenile contribution to the magmas over time (red box in Fig. 7b), dropping from an average of 55% during the Paleo- and Mesoarchean to ~40% at 2.9 Ga, and down to ~20% at around 2.7 Ga. We suggest that the reason for this general trend is a change in geodynamics at 2.9 Ga, with a transition from island arc to continental arc (see discussion in the next section). Additionally, this drop of mantle input coincides with the increase of sediment input to the generation of crustal granitoids as suggested by the O isotope data, (2) we observe some significant variations of the juvenile input during the Paleoarchean, with rapid drops of up to 30% immediately followed by rapid increases. Although similar variations have been interpreted to reflect tectonic switching from regimes dominated by compression punctuated by extensional events (e.g. Collins, 2002; Collins et al., 2011; Kemp et al., 2009a), it is likely that some of these apparent variations of mantle input can simply be an artefact related to the scarcity of the Paleoarchean record, largely underrepresented in this dataset.

Overall, the detrital zircon record indicates a change of geodynamic processes at ca. 2.9 Ga. During the Paleoarchean, processes of renewed juvenile crust generation were operating, and although we have little direct evidence, it was certainly characterized by relatively high mantle contribution to magmatic episodes. At ca. 2.9 Ga there is a net increase in the extent of crustal reworking (further supported by geochemical arguments, Farina et al., 2015) in the transition to a regime with balanced growth and destruction.

5.3. A geodynamic model for the SSFC

The combined dataset of magmatic and detrital zircons indicates that the SSFC was continuously affected by magmatic activity from ca. 3.50 to 2.65 Ga. Any geodynamic model chosen to represent the evolution of this portion of the crust must account for all of the features within this combined U-Pb-Hf-O dataset, as well as the field, petrographic and geochemical evidence collected by Farina et al. (2015). Below we discuss the magmatic and geodynamic evolution of the SSFC.

5.3.1. Pre-2.9 Ga

The early evolution of the SSFC is represented solely by detrital zircons, displaying continuous and homogeneous subchondritic εHf_t values between ca. 3.5 Ga and 2.9 Ga. The lack of Paleoarchean rocks in the field precludes any precise interpretation on the nature of the crust that was formed at the time. However, similar isotopic values have been described in TTGs from other Archean terranes (Moyen and Martin, 2012). Additionally, the modelling discussed in Section 5.2 indicates that: (1) the majority of the crust (~90%) was originally formed before 2.9 Ga, and (2) the juvenile proportion of newly formed crust averages ~55% over that period, before decreasing notably after 2.9 Ga. Evidence is missing however in the SSFC to further discuss Paleoarchean tectonics and to explain the long-lived production of juvenile continental crust in the SSFC.

5.3.2. Post-2.9 Ga

The proposed Neoarchean evolution model comprises two stages, the first one coincides with the RVI and RVII events, and the second one corresponds to the Mamona event.

During *stage I* (Fig. 8a), the model must account for: (1) reworking of Paleoarchean felsic crust evidenced by older model ages in post-2.9 Ga magmas, the erosion and deposition of this crust into Neoarchean and Paleoproterozoic sedimentary basins, (2) the general geochemical trends indicating a progressive HFSE enrichment of the source of these magmas, (3) lesser juvenile contribution to the magmatism, and (4) the systematic differences (field, geochemical and isotopic) observed between the three complexes. These data can be reconciled with a continental collision model, during which the accretion of various proto-continents leads to a tectonically thickened crust which undergoes progressive reworking. This scenario also accounts for the metamorphic event between 2.78 and 2.73 Ga recorded in the SSFC (Farina et al., 2015; Lana et al., 2013).

Following this episode of crustal thickening, we suggest that *stage II* (Fig. 8b) marks a modification of the tectonic regime into extensional or non-compressional settings, during which slab break-off or retreat,

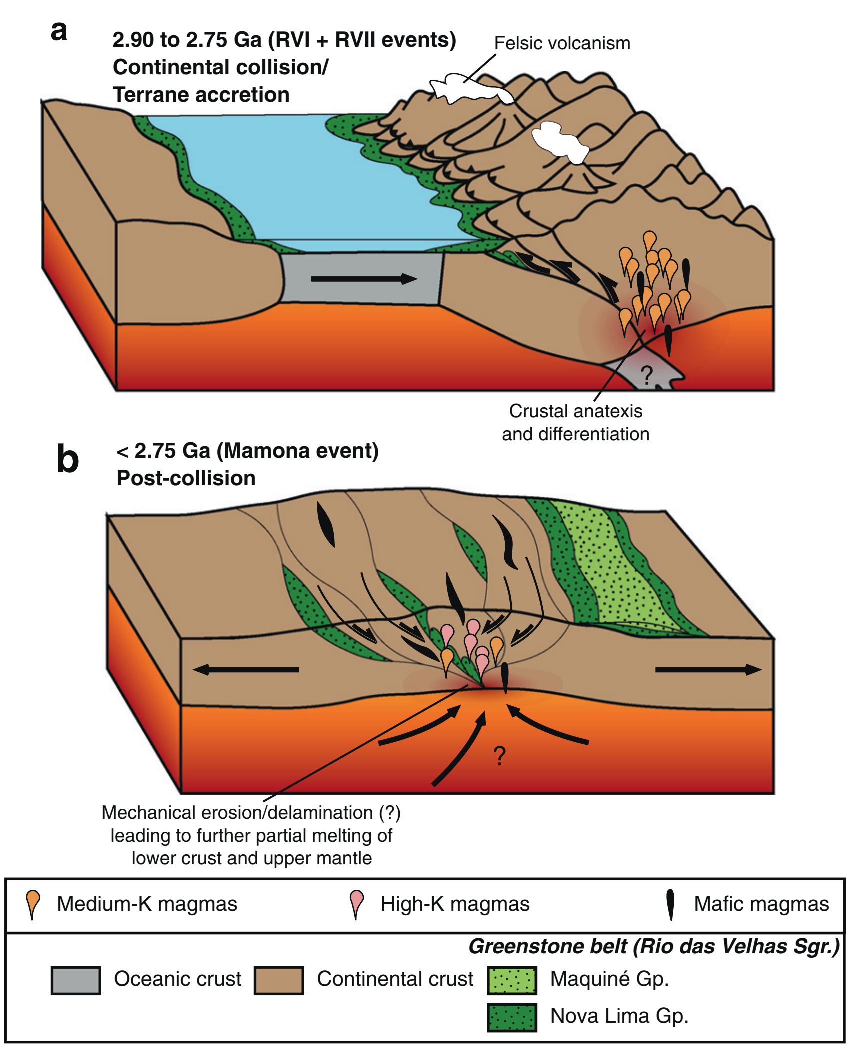

Fig. 8. Sketch illustrating the evolution of the Archean continental crust exposed in the SSFC. The diagrams are explained in more details in Section 5.3. (a) From 2.9 Ga, the accretion of several proto-continents progressively leads to a tectonically thickened continental nucleus that undergoes differentiation, producing the medium-K magmas characteristic for the RVI and RVII events. The felsic volcanism associated with RVII is recorded in the greenstone belt sequence; (b) During the post-collisional Mamona event (<2.75 Ga), the induced inflow of asthenospheric mantle beneath the orogenic prism triggers further melting of lower crustal and upper mantle lithologies.

lithospheric delamination or late- to post-orogenic gravitational collapse can trigger further melting of lower crustal lithologies (e.g. Duretz and Gerya, 2013; van Hunen and Allen, 2011). In this scenario, the compression of local geotherms at the base of the crust promotes renewed partial melting and regional metamorphism of the lower crust (Sandiford and Powell, 1986) and upper mantle. This is further supported by the existence of mafic-intermediate amphibolitic dikes emplaced during this time. We suggest that the magmatism produced during this event generates three types of granitoids. First, the local remelting of older (RVI and RVII) gneisses (the medium-K magmas of Farina et al., 2015) generates small volumes of magmas with a wide range of compositions reflecting the compositional and isotopic heterogeneity of the source(s). These rocks are currently exposed in all three complexes as decimetre- to meter-scale granitic veins and dikes, small plutons (General Carneiro, Santa Luzia, Ibirité, Brumadinho) and domains closely associated with the gneisses as well as leucocratic veins and dikes. Secondly, in the Bonfim complex, the reworking at depth of metasediments produced large volumes of biotite and two-mica granitoids (Mamona and Souza Noschese batholiths). And finally in the Belo Horizonte complex, the generation of the Pequi and Florestal batholiths primarily reflects the remelting of a metabasaltic source, generating magmas that later assimilated some older crust. This final event is synchronous with the complete depletion of the lower crust in heat-producing elements and the subsequent stabilization of the SSFC (Lana et al., 2013; Romano et al., 2013; Sandiford and McLaren, 2002).

Such a scenario has been proposed for a number of analogous Archean terranes such as for example the Yilgarn and Greenland cratons, interpreted as collages of several crustal blocks formed during arc magmatism, terrane accretion and collisional orogeny (e.g. Czarnota et al., 2010; Windley and Garde, 2009). Additionally, Laurent et al. (2014) recently reviewed the temporal evolution of several well-characterized Archean terranes, identifying a two-stage sequence. First, a long-lived period of TTG magmatism, followed by the generation of a range of more enriched granitoids emplaced during a shorter event. These authors tentatively proposed that this pattern reflects a global geodynamic model of subduction and subsequent continental collision, taking place on a planetary scale between 3.0 and 2.5 Ga, as a result of the progressive cooling of the Earth. The zircon dataset presented in this study can easily be reconciled with such scenario, although it does not provide direct evidence for it. 2.9 Ga marks a clear transition in the SSFC into a period where crustal reworking has dominated over net juvenile magmatic additions. By analogy, we infer that this change relates to the onset of accretionary and collisional events in the SSFC, leading to oceanic closure and progressive amalgamation of Paleoarchean proto-continental blocks.

6. Conclusion

The conclusions that arise from this U-Pb-Hf-O isotope study on Neoarchean granitoids and gneisses from the SSFC are as follows:

- Samples from the three complexes (Bação, Bonfim and Belo Horizonte) plot on distinct crustal evolution arrays, suggesting the involvement of Paleoarchean crust in their generation, which occurs via different processes (remelting, mixing, assimilation and/or source contamination). Combined with field data, this suggests that these complexes represent terranes with different identities (different proto-continents and/or levels of the crust) accreted together during a late collisional stage.
- The present Hf dataset combined with whole-rock geochemistry indicates: (1) a continuous differentiation trend from sodic (medium-K) to potassic (high-K) magmatism with age, reflecting progressive enrichment of the source in HFSE and probable shallowing of the depth of melting, and (2) that Hf isotopes alone do not represent the diversity of rocks and processes evidenced here.
- isotope results indicate: (1) a secular trend towards high $\delta^{18}O$ values confirming the involvement of metasediments in the petrogenesis of Neoarchean high-K granitoids, (2) the presence of upper-crustal level hydrothermal systems during the Meso- and Neoarchean magmatism in the SSFC.
- Isotopic modelling, based on available Hf from detrital zircons record complements this dataset, indicating a major change in the evolution of the SSFC at 2.9 Ga. This change marks the transition between a Paleoarchean regime possibly dominated by TTG production and net crustal growth, and a Neoarchean regime that is dominated by reworking processes, producing a wide variety of granitoid magmas with highly scattered radiogenic isotope compositions. We attribute this transition to the onset of continental collision in the SSFC.

Acknowledgments

This paper was supported by CNPq (grant numbers: 401334/2012-0; 402852/2012-5 and 302633/2011-1) and FAPEMIG (grant numbers: APQ03943 and RDP 0067-10) grants. We thank Rafael Romano for providing his sample mounts. Thanks to Ana Maria Saldarriago for picking and CL imaging grains at Portsmouth and for O isotope analysis at Edinburgh. Elena Belousova and an anonymous reviewer are thanked for their valuable and constructive comments which improved the manuscript. Nelson Eby is acknowledged for his editorial handling.

Appendix A. Supplementary data

Supplementary data to this article can be found online at http://dx.doi.org/10.1016/j.lithos.2016.09.029.

References

Alkmim, F.F., Marshak, S., 1998. The Transamazonian orogeny in the Quadrilátero-Ferrífero, Minas Gerais, Brazil: Paleoproterozoic collision and collapse in the Souhtern São Francisco Craton region. Precambrian Research 90, 29–58.
Almeida, F.F.M., Hasui, Y., Brito Neves, B.B., Fuck, R.A., 1981. Brazilian structural provinces: an introduction. Earth Science Reviews 17, 1–29.
Amelin, Y., Lee, D.-C., Halliday, A.N., 2000. Early-middle Archaean crustal evolution deduced from Lu–Hf and U–Pb isotopic studies of single zircon grains. Geochimica et Cosmochimica Acta 64, 4205–4225.
Appleby, S.K., Gillespie, M.R., Graham, C.M., Hinton, R.W., Oliver, G.J.H., Kelly, N.M., E.I.M.F, 2010. Do S-type granites commonly sample infracrustal sources? New results from an integrated O, U–Pb and Hf isotope study of zircon. Contributions to Mineralogy and Petrology 160, 115–132.
Barbosa, J.S.F., Sabaté, P., 2004. Archean and Paleoproterozoic crust of the São Francisco craton, Bahia, Brazil: geodynamic features. Precambrian Research 133, 1–27.
Belousova, E.A., Kostitsyn, Y.A., Griffin, W.L., Begg, G.C., O'Reilly, S.Y., Pearson, N.J., 2010. The growth of the continental crust: constraints from zircon Hf-isotope data. Lithos 119, 457–466.
Bennett, V.C., DePaolo, D.J., 1987. Proterozoic crustal history of the western United States as determined by neodymium isotopic mapping. Geological Society of America Bulletin 99, 674–685.
Bindeman, I.N., 2011. When do we need pan-global freeze to explain 18-O depleted zircons and rocks? Geology 39, 799–800.
Bindeman, I.N., Valley, J.W., 2001. Low- δ18O rhyolites from Yellowstone: magmatic evolution based on analyses of zircons and individual phenocrysts. Journal of Petrology 42, 1491–1517.
Bindeman, I.N., Fu, B., Kita, N., Valley, J.W., 2008. Origin and evolution of silicic magmatism at Yellowstone based on ion microprobe analysis of isotopically zoned zircons. Journal of Petrology 49, 163–193.
Blichert-Toft, J., Puchtel, I.S., 2010. Depleted mantle sources through time: evidence from Lu–Hf and Sm–Nd isotope systematics of Archean komatiites. Earth and Planetary Science Letters 297 (3–4), 598–606.
Boekhout, F., Roberts, N.M., Gerdes, A., Schaltegger, U., 2013. A Hf-isotope perspective on continent formation in the south Peruvian Andes. In: Roberts, N.M.W., Van Kranendonk, M., Parman, S., Shirey, S., Clift, P.D. (Eds.), Continent Formation Through Time. Geological Society, London, Special Publications 389.
Campos, J.C.S., Carneiro, M.A., Basei, M.A.S., 2003. U-Pb evidence for Late Neoarchean crustal reworking in the southern São Francisco Craton (Minas Gerais, Brazil). Anais da Academia Brasileira de Ciências 75 (4), 497–511.
Carneiro, M.A., 1992. O Complexo Metamórfico Bonfim Setentrional (Quadrilátero Ferrífero, Minas Gerais): Litoestratigrafia e evolução geológica de um segmento de crosta continental do Arqueano. Unpublished PhD Thesis. University of São Paulo, Brazil, p. 233.

Carneiro, M.A., Jordt-Evangelista, H., Teixeira, W., 1997. Eventos Magmaticos Arqueanos de Natureza Calcio-alcalina e Tholeiitica no Quadrilatero Ferrifero e suas Implicações Tectonicas. Revista Brasileira de Geociencias 27, 121–128.

Cavosie, A.J., Valley, J.W., Wilde, S.A., E.I.M.F, 2005. Magmatic δ18O in 4400–3900 Ma detrital zircons: a record of the alteration and recycling of crust in the Early Archean. Earth and Planetary Science Letters 235, 663–681.

Collins, W.J., 2002. Hot orogens, tectonic switching, and creation of continental crust. Geology 30, 535–538.

Collins, W.J., Belousova, E.A., Kemp, A.I.S., Murphy, J.B., 2011. Two contrasting Phanerozoic orogenic systems revealed by hafnium isotope data. Nature Geoscience 4 (5), 333–337.

Czarnota, K., Champion, D.C., Goscombe, B., Blewett, R.S., Cassidy, K.F., Henson, P.A., Groenewald, P.B., 2010. Geodynamics of the Eastern Yilgarn Craton. Precambrian Research 183, 175–202.

Dhuime, B., Hawkesworth, C.J., Cawood, P.A., Storey, C.D., 2012. A change in the geodynamics of continental growth 3 billion years ago. Science 335, 1334–1336.

Dorr II, J.V.N., 1969. Physiographic, Stratigraphic and Structural Development of the Quadrilátero Ferrífero, Minas Gerais, Brazil. USGS/DNPM, Washington, Professional Paper 641-A (110 pp.).

Duretz, T., Gerya, T.V., 2013. Slab detachment during continental collision: influence of crustal rheology and interactions with lithospheric delamination. Tectonophysics 602, 124–140.

Eiler, J.M., 2001. Oxygen isotope variations of basaltic lavas and upper mantle rocks. In: Valley, J.W., Cole, D.R. (Eds.), Stable Isotope GeochemistryReviews in Mineralogy and Geochemistry 43. Mineralogical Society of America/Geochemical Society, Washington, DC, pp. 319–364.

Farina, F., Stevens, G., Gerdes, A., Frei, D., 2014. Small-scale Hf isotopic variability in the Peninsula pluton (South Africa): the processes that control inheritance of 176Hf/177Hf diversity in S-type granites. Contributions to Mineralogy and Petrology 168, 1065.

Farina, F., Albert, C., Lana, C., 2015. The Neoarchean transition between medium- and high-K granitoids: clues from the Southern São Francisco Craton (Brazil). Precambrian Research 266, 375–394.

Farina, F., Albert, C., Martínez Dopico, C., Aguilar Gil, C., Moreira, H., Hippertt, J.P., Cutts, K., Alkmim, F.F., Lana, C., 2016. The Archean-Paleoproterozoic evolution of the Quadrilatero Ferriferro (Brasil): current models and open questions. Journal of South American Earth Sciences 68, 4–21.

Gerdes, A., Zeh, A., 2006. Combined U–Pb and Hf isotope LA-(MC-)ICP-MS analyses of detrital zircons: comparison with SHRIMP and new constraints for the provenance and age of an Armorican metasediment in central Germany. Earth and Planetary Science Letters 249, 47–61.

Gerdes, A., Zeh, A., 2009. Zircon formation versus zircon alteration – new insights from combined U–Pb and Lu–Hf in-situ LA–ICP–MS analyses, and consequences for the interpretation of Archean zircon from the Central Zone of the Limpopo Belt. Chemical Geology 261, 230–243.

Gregory, R.T., 1991. Oxygen history of seawater revisited: timescales for boundary event changes in the oxygen isotope composition of seawater. In: Taylor, H.P., et al. (Eds.), Stable Isotope Geochemistry. Lancaster Press, San Antonio, Texas, pp. 65–76.

Gilliam, C.E., Valley, J.W., 1997. Low δ18O magma, Isle of Skye, Scotland; evidence from zircons. Geochimica et Cosmochimica Acta 61, 4975–4981.

Griffin, W.L., Belousova, E.A., Shee, S.R., Pearson, N.J., O'Reilly, S.Y., 2004. Archean crustal evolution in the northern Yilgarn Craton: U–Pb and Hf-isotope evidence from detrital zircons. Precambrian Research 131, 231–282.

Griffin, W.L., Belousova, E.A., O'Neill, C., O'Reilly, S.Y., Malkovets, V., Pearson, N.J., Spetsius, S., Wilde, S.A., 2014. The world turns over: Hadean-Archean crust- mantle evolution. Lithos 189, 2–15.

Guitreau, M., 2012. Les isotopes de l'Hafnium dans les TTG et leurs zircons: témoins de la croissance des premiers continents Unpublished PhD Thesis Ecole Normale Supérieure de Lyon, France.

Hartmann, L.A., Endo, I., Suita, M.T.F., Santos, J.O.S., Frantz, J.C., Carneiro, M.A., Naughton, N.J., Barley, M.E., 2006. Provenance and age delimitation of Quadrilátero Ferrífero sandstones based on zircon U–Pb isotopes. Journal of South American Earth Sciences 20, 273–285.

Hiess, J., Bennett, V.C., Nutman, A.P., Williams, I.S., 2011. Archaean fluid-assisted crustal cannibalism recorded by low δ18O and negative εHf(T) isotopic signatures of West Greenland granite zircon. Contributions to Mineralogy and Petrology 161, 1027–1050.

Hollis, J.A., Van Kranendonk, M.J., Cross, A.J., Kirkland, C.L., Armstrong, R.A., Allen, C.M., 2014. Low δ18O zircon grains in the Neoarchean Rum Jungle Complex, northern Australia: an indicator of emergent continental crust. Lithosphere 6, 17–25.

Hoskin, P.W.O., Black, L.P., 2000. Metamorphic zircon formation by solid-state recrystallization of protolith igneous zircon. Journal of Metamorphic Geology 18, 423–439.

Ivanic, T.J., Van Kranendonk, M.J., Kirkland, C.L., Wyche, S., Wingate, M.T.D., Belousova, E.A., 2012. Zircon Lu-Hf isotopes and granite geochemistry of the Murchison Domain of the Yilgarn Craton: evidence for reworking of Eoarchean crust during Meso-Neoarchean plume-driven magmatism. Lithos 148, 112–127.

Kelemen, P., Hanghoj, K., Greene, A., 2003. One view of the geochemistry of subduction-related magmatic arcs, with an emphasis on primitive andesite and lower crust. In: Holland, H., Turekian, K. (Eds.), Treatise on Geochemistry 3. Elsevier-Pergammon, Oxford, pp. 1–70.

Kemp, A.I.S., Hawkesworth, C.J., Paterson, B.A., Kinny, P.D., 2006. Episodic growth of the gondwana supercontinent from hafnium and oxygen isotopes in zircon. Nature 439, 580–583.

Kemp, A.I.S., Hawkesworth, C.J., Foster, G.L., Paterson, B.A., Woodhead, J.D., Hergt, J.M., Gray, C.M., Whitehouse, M.J., 2007. Magmatic and crustal differentiation history of granitic rocks from Hf–O isotopes in zircon. Science 315 (5814), 980–983.

Kemp, A.I.S., Hawkesworth, C.J., Collins, W.J., Gray, C.M., Blevin, P.L., 2009a. Isotopic evidence for rapid continental growth in an extensional accretionary orogen: the Tasmanides, eastern Australia. Earth and Planetary Science Letters 284, 455–466.

Kemp, A.I.S., Foster, G.L., Scherstén, A., Whitehouse, M.J., Darling, J., Storey, C., 2009b. Concurrent Pb–Hf isotope analysis of zircon by laser ablation multi-collector ICP-MS, with implications for the crustal evolution of Greenland and the Himalayas. Chemical Geology 261, 244–260.

Kita, N.T., Ushikubo, T., Fu, B., Valley, J.W., 2009. Hihg precision SIMS oxygen isotope analysis and the effect of sample topography. Chemical Geology 264, 43–57.

Koglin, N., Zeh, A., Cabral, A.R., Gomes Jr., A.A.S., Corrêa Neto, A.V., Brunetto, W.J., Galbiatti, H., 2014. Depositional age and sediment source of the auriferous Moeda Formation, Quadrilatero Ferrifero of Minas Gerais, Brazil: new constraints from U-Pb-Hf isotopes in zircon and xenotime. Precambrian Research 255, 96–108.

Lana, C., Alkmim, F.F., Armonstrong, R., Scholz, R., Romano, R., Nalini Jr., H.R., 2013. The ancestry and magmatic evolution of Archaean TTG rocks of the Quadrilátero Ferrífero province, Southeast Brazil. Precambrian Research 231, 157–173.

Lancaster, P.J., Storey, C.D., Hawkesworth, C.J., 2014. The Eoarchean foundation of the North Atlantic Craton. In: Roberts, N.M.W., Van Kranendonk, M., Parman, S., Shirey, S., Clift, P.D. (Eds.), Continent Formation Through Time. Geological Society, London, Special Publications 389.

Lancaster, P.J., Dey, S., Storey, C.D., Mitra, A., Bhunia, R.K., 2015. Contrasting crustal evolution processes in the Dharwar craton: insights from detrital zircon U-Pb and Hf isotopes. Gondwana Research 28, 1361–1372.

Laurent, O., Martin, H., Moyen, J.-F., Doucelance, R., 2014. The diversity and evolution of late-Archean granites: evidence for the onset of a "modern-style" plate tectonics between 3.0 and 2.5 Ga. Lithos 205, 208–235.

Lobato, L.M., Ribeiro-Rodrigues, L.C., Vieira, F.W.R., 2001. Brazil's premier gold province. Part II: geology and genesis of gold deposits in the Archean Rio das Velhas Greenstone belt, Quadrilátero Ferrífero. Mineralium Deposita 36, 249–277.

Longstaffe, F.J., Schwarcz, H.P., 1977. 18O/16O of Archean clastic metasedimentary rocks: a petrogenetic indicator for Archean gneisses? Geochimica et Cosmochimica Acta 41, 1303–1312.

Ludwig, K.R., 2003. Isoplot/Ex Version 3.00: A Geochronological Toolkit for MicrosoftExcel. Berkeley Geochronology Center, Berkeley, CA.

Machado, N., Carneiro, M.A., 1992. U–Pb evidence of late Archean tectono-thermal activity in the southern São Francisco shield, Brazil. Canadian Journal of Earth Sciences 29, 2341–2346.

Machado, N., Noce, C.M., Ladeira, E.A., Belo de Oliveira, O.A., 1992. U–Pb geochronology of Archean magmatism and Proterozoic metamorphism in the Quadrilátero Ferrífero, Southern São Francisco craton, Brazil. Geological Society of America Bulletin 104, 1221–1227.

Machado, N., Schrank, A., Noce, C.M., Gauthier, G., 1996. Ages of detrital zircon from Archean-Paleoproterozoic sequences: implications for Greenstone Belt setting evolution of a Transamazonian foreland basin in Quadrilátero Ferrífero, southeast Brazil. Earth and Planetary Science Letters 141, 259–276.

Marshak, S., Alkmim, F.F., Jordt Evangelista, H., 1992. Proterozoic crustal extension and the generation of dome-and-keel structure in an Archean granite–greenstone terrane. Nature 397, 491–493.

Marshak, S., Tinkham, D., Alkmim, F.F., Brueckner, H., Bornhorst, T., 1997. Dome-and-keel provinces formed during Paleoproterozoic orogenic collapse – diapir clusters, core complexes, or neither? Examples from the Quadrilatero Ferrifero (Brazil) and the Penokean Orogen (USA). Geology 25, 415–418.

Monani, S., Valley, J.W., 2001. Oxygen isotope ratios of zircon: magma genesis of low δ18O granites from the British Tertiary igneous province, western Scotland. Earth and Planetary Science Letters 184, 377–392.

Moreira, H., Lana, C., Nalini Jr., H.A., 2016. The detrital zircon record of an Archaean convergent basin in the Southern São Francisco Craton, Brazil. Precambrian Research 275, 84–99.

Moyen, J.F., 2011. The composite Archaean grey gneisses: petrological significance, and evidence for a non-unique tectonic setting for Archaean crustal growth. Lithos 123 (1–4), 21–36.

Moyen, J.F., Martin, H., 2012. Forty years of TTG research. Lithos 148, 312–336.

Murakami, T., Chakoumakos, B.C., Ewing, R.C., Lumpkin, G.R., Weber, W.J., 1991. Alpha-decay event damage in zircon. American Mineralogist 76, 1510–1532.

Naeraa, T., Scherstein, A., Rosing, M.T., Kemp, A.I.S., Hofmann, J.E., Koldelt, T.F., Whitehouse, M.J., 2012. Hafnium isotope evidence for a transition in the dynamics of continental growth 3.2 Ga ago. Nature 485, 627–630.

Nebel, O., Nebel-Jacobsen, Y., Mezger, K., Berndt, J., 2007. Initial Hf isotope compositions in magmatic zircon from early Proterozoic rocks from the Gawler Craton, Australia: a test for zircon model ages. Chemical Geology 241, 27–37.

Noce, C.M., Machado, N., Teixeira, W., 1998. U–Pb geochronology of gneisses and granitoids in the Quadrilátero Ferrífero (southern São Francisco craton): age constraints for Archean and Paleoproterozoic magmatism and metamorphism. Revista Brasileira de Geociencias 28, 95–102.

Noce, C.M., Zuccheti, M., Baltazar, O.F., Armstrong, R., Dantas, E., Renger, F.E., Lobato, L.M., 2005. Age of felsic volcanism and the role of ancient continental crust in the evolution of the Neoarchean Rio das Velhas greenstone belt (Quadrilátero Ferrífero, Brazil): U–Pb zircon dating of volcaniclastic graywackes. Precambrian Research 141, 67–82.

Patchett, P.J., Arndt, N.T., 1986. Nd isotopes and tectonics of 1.9–1.7 Ga crustal genesis. Earth and Planetary Science Letters 78, 329–338.

Payne, J.L., McInerney, D.J., Barovich, K.M., Kirkland, C.L., Pearson, N.J., Hand, M., 2016. Strengths and limitations of zircon Lu-Hf and O isotopes in modelling crustal growth. Lithos 248-251, 175–192.

Peck, W.H., King, E.M., Valley, J.V., 2000. Oxygen isotope perspective on Precambrian crustal growth and maturation. Geology 28, 363–366.

Pietranik, A.B., Hawkesworth, C.J., Storey, C.D., Kemp, A.I.S., Sircombe, K.N., Whitehouse, M.J., Bleeker, W., 2008. Episodic mafic crust formation from 4.5–2.8 Ga: new evidence from detrital zircons, Slave Craton, Canada. Geology 36, 875–878.

Rapp, R.P., Watson, E.B., 1995. Dehydration melting of metabasalt at 8-32 kbar: implications for continental growth and crust-mantle recycling. Journal of Petrology 36, 891–931.

Roberts, N.M.W., Spencer, C.J., 2014. The Zircon Archive of Continent Formation Through Time, Geological Society, London, Special Publications.

Romano, R., Lana, C., Alkmim, F.F., Stevens, G.S., Armstrong, R., 2013. Stabilization of the southern portion of the São Francisco Craton, SE Brazil, through a long-lived period of potassic magmatism. Precambrian Research 224, 143–159.

Sandiford, M., McLaren, S., 2002. Tectonic feedback and the ordering of heat producing elements within the continental lithosphere. Earth and Planetary Science Letters 204, 133–150.

Sandiford, M., Powell, R., 1986. Deep crustal metamorphism during continental extension: ancient and modern examples. Earth and Planetary Science Letters 79, 151–158.

Satkoski, A.M., Bickford, M.E., Samson, S.D., Bauer, R.L., Mueller, P.A., Kamenov, G.D., 2013. Geochemical and Hf–Nd isotopic constraints on the crustal evolution of Archean rocks from the Minnesota River Valley, USA. Precambrian Research 224, 36–50.

Taylor, S.R., 1977. Island arc models and the composition of the continental crust. In: Talwani, M., Pitman III, W.C. (Eds.), Island Arcs, Deep Sea Trenches, and Back-Arc Basins, Maurice Ewing Ser. 1. AGU, Washington D.C., pp. 325–335.

Teixeira, W., Figueiredo, M.C.H., 1991. An outline of Early Proterozoic crustal evolution in the São Francisco Craton, Brazil: a review. Precambrian Research 53, 1–22.

Teixeira, W., Carneiro, M.A., Noce, C.A., Machado, N., Sato, K., Taylor, P.N., 1996. Pb, Sr and Nd isotope constraints on the Archean evolution of gneissic granitoid complexes in the southern São Francisco Craton, Brazil. Precambrian Research 78, 151–164.

Valley, J.W., 2003. Oxygen isotopes in zircon. Reviews in Mineralogy and Geochemistry 53, 343–385.

Valley, J.W., Chiarenzelli, J.R., McLelland, J.M., 1994. Oxygen isotope geochemistry of zircon. Earth and Planetary Science Letters 126, 187–206.

Valley, J.W., Kinny, P.D., Schulze, D.J., Spicuzza, M.J., 1998. Zircon megacrysts from kimberlite: oxygen isotope variability among mantle melts. Contributions to Mineralogy and Petrology 133, 1–11.

Valley, J.W., Lackey, J.S., Cavosie, A.J., Clechenko, C.C., Spicuzza, M.J., Basei, M.A.S., Bindeman, I.N., Ferreira, V.P., Sial, A.N., King, E.M., Peck, W.H., Sinha, A.K., Wei, C.S., 2005. 4.4 billion years of crustal maturation: oxygen isotope ratios of magmatic zircon. Contributions to Mineralogy and Petrology 150, 561–580.

Van Achterbergh, E., Ryan, C.G., Jackson, S.E., Griffin, W., 2001. Data reduction soft- ware for LA-ICP-MS. In: Sylvester, P. (Ed.)Laser Ablation ICPMS in the Earth Science 29. Mineralogical Association of Canada, pp. 239–243.

van Hunen, J., Allen, M.B., 2011. Continental collision and slab break-off: a comparison of 3-D numerical models with observations. Earth and Planetary Science Letters 302 (1–2), 27–37.

Veizer, J., Mackenzie, F.T., 2003. Evolution of sedimentary rocks. Treatise on Geochemistry 7, 369–407.

Villaros, A., Buick, I.S., Stevens, G., 2012. Isotopic variations in S-type granites: an inheritance from a heterogeneous source? Contributions to Mineralogy and Petrology 163, 243–257.

Wiedenbeck, M., Hanchar, J.M., Peck, W.H., Sylvester, P., Valley, J., Whitehouse, M., Kronz, A., Morishita, Y., Nasdala, L., Fiebig, J., Franchi, I., Girard, J.-P., Greenwood, R.C., Hinton, R., Kita, N., Mason, P.R.D., Norman, M., Ogasawara, M., Piccoli, P.M., Rhede, D., Satoh, H., Schulz-Dobrick, B., Skar, O., Spicuzza, M.J., Terada, K., Tindle, A., Togashi, S., Vennemann, T., Xie, Q., Zheng, Y.-F., 2004. Further characterization of the 91500 zircon crystal. Geostandards and Geoanalytical Research 28, 9–39.

Windley, B.F., Garde, A.A., 2009. Arc-generated blocks with crustal sections in the North Atlantic craton of West Greenland: crustal growth in the Archean with modern analogues. Earth-Science Reviews 93, 1–30.

Workman, R.K., Hart, S.R., 2005. Major and trace element composition of the depleted MORB mantle (DMM). Earth and Planetary Science Letters 231 (1–2), 53–72.

Wotslaw, J.-F., Bindeman, I.N., Schaltegger, U., Brooks, C.K., Naslund, H.R., 2012. High-resolution insights into episodes of crystallization, hydrothermal alteration and remelting in the Skaergaard intrusive complex. Earth and Planetary Science Letters 355-356, 199–212.

Zeh, A., Gerdes, A., Barton Jr., J.M., 2009. Archean accretion and crustal evolution of the Kalahari Craton – the zircon age and Hf isotope record of granitic rocks from Barberton/Swaziland to the Francistown Arc. Journal of Petrology 50, 933–966.

Zeh, A., Stern, R.A., Gerdes, A., 2014. The oldest zircons of Africa – their U-Pb-Hf-O isotope and trace element systematics, and implications for Hadean to Archean crust-mantle evolution. Precambrian Research 241, 203–230.